

*Journal of*  
***Mechanics of***  
***Materials and Structures***

**A STUDY OF PENALTY FORMULATIONS USED IN THE  
NUMERICAL APPROXIMATION OF A RADIALY SYMMETRIC  
ELASTICITY PROBLEM**

Adair R. Aguiar, Roger L. Fosdick and Jesús A. G. Sánchez

***Volume 3, Nº 8***

***October 2008***



## A STUDY OF PENALTY FORMULATIONS USED IN THE NUMERICAL APPROXIMATION OF A RADIALY SYMMETRIC ELASTICITY PROBLEM

ADAIR R. AGUIAR, ROGER L. FOSDICK AND JESÚS A. G. SÁNCHEZ

We consider a class of two-dimensional problems in classical linear elasticity for which material overlapping occurs in the absence of singularities. Of course, material overlapping is not physically realistic, and one possible way to prevent it uses a constrained minimization theory. In this theory, a minimization problem consists of minimizing the total potential energy of a linear elastic body subject to the constraint that the deformation field must be locally invertible. Here, we use an interior and an exterior penalty formulation of the minimization problem together with both a standard finite element method and classical nonlinear programming techniques to compute the minimizers. We compare both formulations by solving a plane problem numerically in the context of the constrained minimization theory. The problem has a closed-form solution, which is used to validate the numerical results. This solution is regular everywhere, including the boundary. In particular, we show numerical results which indicate that, for a fixed finite element mesh, the sequences of numerical solutions obtained with both the interior and the exterior penalty formulations converge to the same limit function as the penalization is enforced. This limit function yields an approximate deformation field to the plane problem that is locally invertible at all points in the domain. As the mesh is refined, this field converges to the exact solution of the plane problem.

### 1. Introduction

There are problems in the classical linear theory of elasticity whose closed form solutions, while satisfying the governing equations of equilibrium together with well-posed boundary conditions, allow material overlapping to occur. Typically, problems of this kind involve some sort of singularity, and strains exceeding a level acceptable from the point of view of a linear theory occur around the singular points [Aguilar and Fosdick 2001; Aguiar 2006]. But this is not always the case, as we shall show in this work.

We consider a two-dimensional problem in classical linear elasticity for which material overlapping occurs in the absence of singularities. The problem concerns the equilibrium of a circular homogeneous and anisotropic pipe, which is fixed at its inner surface, radially compressed along its outer surface by a uniformly distributed normal pressure, and subjected to an axial force acting on its flat ends. The requirement that the displacement field be radially symmetric with respect to the center of the pipe allows the derivation of a closed-form solution that predicts overlapping of material at the inner surface of the linear elastic pipe when the radial compressive force becomes larger than a critical load, which is small.

One possible way to prevent the anomalous behavior of self-intersection is proposed by Fosdick and Royer-Carfagni [2001]. It combines the linear theory with the constraint of local injectivity through a

---

*Keywords:* anisotropic elasticity, constrained minimization, penalty method, finite element method.

Lagrange multiplier technique. These authors investigate the problem of minimizing the total potential energy  $\mathcal{E}$  of classical linear elasticity on an admissible set  $\mathcal{A}_\varepsilon$  of vector-valued functions  $\mathbf{v}$  that satisfy the injectivity constraint  $\det(\mathbf{1} + \nabla \mathbf{v}) \geq \varepsilon > 0$  for a sufficiently small  $\varepsilon \in \mathbb{R}$ . In particular, they show the existence of a solution for the constrained minimization problem in two dimensions. The constrained problem is, however, highly nonlinear and, in general, needs to be solved numerically.

Obeidat et al. [2001] and Aguiar [2006] present finite element approaches to solve this class of constrained problems. In the former, a carefully designed algorithm is required to keep track of all subdomains of the reference configuration where the injectivity constraint is violated.

The approach in [Aguiar 2006] is based on an *interior penalty formulation*, which consists of replacing  $\mathcal{E}$  by a penalized functional  $\mathcal{E}_\gamma = \mathcal{E} + \mathcal{Q}/\gamma$ , where  $\gamma$  is an arbitrary positive number and  $\mathcal{Q}$  is a penalty functional defined on the constraint set  $\mathcal{A}_\varepsilon$ . The penalty functional is nonnegative on  $\mathcal{A}_\varepsilon$ , satisfies  $\mathcal{Q}[\mathbf{v}] \rightarrow \infty$  as  $\mathbf{v}$  approaches the boundary of  $\mathcal{A}_\varepsilon$ , and is designed so that minimizers of  $\mathcal{E}_\gamma[\cdot]$  lie in the interior of the constraint set  $\mathcal{A}_\varepsilon$ ; hence the term *interior penalty method*. Thus, the penalty formulation of the constrained problem consists of finding  $\mathbf{u}_\gamma \in \mathcal{A}_\varepsilon$  that minimizes the penalized functional  $\mathcal{E}_\gamma$  over the constraint set  $\mathcal{A}_\varepsilon$ .

In this work, we consider an *exterior penalty formulation*, which consists of replacing  $\mathcal{E}$  by a penalized functional  $\mathcal{E}_\delta = \mathcal{E} + \mathcal{P}/\delta$ , where  $\delta$  is an arbitrary positive number and  $\mathcal{P}$  is a penalty functional defined on the whole set  $\mathcal{A}$ . The penalty functional is nonnegative on  $\mathcal{A}$  and vanishes on  $\mathcal{A}_\varepsilon$ . Thus, the penalty formulation of the constrained problem consists of finding  $\mathbf{u}_\delta \in \mathcal{A}$  that minimizes the penalized functional  $\mathcal{E}_\delta$  over the set  $\mathcal{A}$ . This method has the advantage of yielding an unconstrained minimization problem. In general, the minimizers of  $\mathcal{E}_\delta[\cdot]$  lie in the exterior of the constraint set  $\mathcal{A}_\varepsilon$ ; hence the term *exterior penalty method*. In this work, however, numerical results shown in Section 5 indicate that the minimizers of  $\mathcal{E}_\delta$  for the class of problems considered in Section 3 lie in the interior of  $\mathcal{A}_\varepsilon$  for sufficiently small  $\delta$ . It is not known whether this is to be generally expected.

In Section 2 we apply both penalty formulations on the class of constrained minimization problems considered by Fosdick and Royer-Carfagni [2001]. In Section 3 we present some exact results concerning the compressed pipe problem in the context of both the unconstrained and the constrained theories. For this, we assume that the problem is radially symmetric, which yields a one-dimensional problem for the determination of the radial displacement in the pipe. In Section 4 we use the finite element method to obtain discrete problems from the interior and exterior penalty formulations of the constrained pipe problem and discuss briefly a solution strategy presented by Aguiar [2006]. The resulting numerical scheme is simple to implement, and can be applied in the numerical solution of problems in any dimension. In particular, we apply the numerical scheme in the approximate solution of the one-dimensional problem with the injectivity constraint. Fosdick et al. [2008] use the numerical strategy of Aguiar [2006] to solve the pipe problem in the full two-dimensional setting. For certain values of the shear modulus of the material, their numerical solution is very different from the solution of the one-dimensional problem. This shows that, depending on the elastic parameters, the constrained minimization problem may have more than one solution. In this work, we investigate the one-dimensional problem, because our primary goal is to compare both penalty formulations. Thus, in Section 5 we compare the numerical results obtained from the solutions of the discrete problems using the interior and the exterior penalty methods with the analytical results obtained from the closed-form solution of the constrained minimization problem considered in Section 3. In Section 6 we present some concluding remarks.

### 2. The penalty functional formulation

Let  $\mathcal{B} \subset \mathbb{R}^2$  be the undistorted natural reference configuration of a body. Points  $\mathbf{x} \in \mathcal{B}$  are mapped to points  $\mathbf{y} = \mathbf{f}(\mathbf{x}) \equiv \mathbf{x} + \mathbf{u}(\mathbf{x}) \in \mathbb{R}^2$ , where  $\mathbf{u}(\mathbf{x})$  is the displacement of  $\mathbf{x}$ . The boundary  $\partial\mathcal{B}$  of  $\mathcal{B}$  is composed of two nonintersecting parts,  $\partial_1\mathcal{B}$  and  $\partial_2\mathcal{B}$ ,  $\partial_1\mathcal{B} \cup \partial_2\mathcal{B} = \partial\mathcal{B}$ ,  $\partial_1\mathcal{B} \cap \partial_2\mathcal{B} = \emptyset$ , such that  $\mathbf{u}(\mathbf{x}) = \mathbf{0}$  for  $\mathbf{x} \in \partial_1\mathcal{B}$  and such that a dead load traction field  $\bar{\mathbf{t}}(\mathbf{x})$  is prescribed for  $\mathbf{x} \in \partial_2\mathcal{B}$ . In addition, a body force  $\mathbf{b}(\mathbf{x})$  per unit volume of  $\mathcal{B}$  acts on points  $\mathbf{x} \in \mathcal{B}$ .

We consider the problem of minimum potential energy

$$\min_{\mathbf{v} \in \mathcal{A}_\varepsilon} \mathcal{E}[\mathbf{v}], \quad \mathcal{E}[\mathbf{v}] \equiv \frac{1}{2} a[\mathbf{v}, \mathbf{v}] - f[\mathbf{v}], \tag{1}$$

where

$$a[\mathbf{v}, \mathbf{v}] \equiv \int_{\mathcal{B}} \mathbb{C}[\mathbf{E}] \cdot \mathbf{E} d\mathbf{x}, \quad f[\mathbf{v}] \equiv \int_{\mathcal{B}} \mathbf{b} \cdot \mathbf{v} d\mathbf{x} + \int_{\partial_2\mathcal{B}} \bar{\mathbf{t}} \cdot \mathbf{v} d\mathbf{x}, \tag{2}$$

and  $\mathbf{E} \equiv [\nabla\mathbf{v} + (\nabla\mathbf{v})^T]/2$  is the infinitesimal strain tensor field. The functional  $\mathcal{E}[\cdot]$  is the total potential energy of classical linear theory of elasticity. Furthermore,

$$\mathcal{A}_\varepsilon \equiv \{ \mathbf{v} : W^{1,2}(\mathcal{B}) \rightarrow \mathbb{R}^2 \mid \det(\mathbf{1} + \nabla\mathbf{v}) \geq \varepsilon > 0, \mathbf{v} = \mathbf{0} \text{ almost everywhere on } \partial_1\mathcal{B} \}, \tag{3}$$

is the class of admissible displacement fields and  $\mathbb{C} = \mathbb{C}(\mathbf{x})$  is the elasticity tensor, assumed to be positive definite and totally symmetric. We suppose that  $\varepsilon > 0$  in (3) is sufficiently small.

Fosdick and Royer-Carfagni [2001] fully characterize the solutions of the minimization problem (1)–(3). In particular, they show that there exists a solution to this problem and they derive first variation conditions for a minimizer  $\mathbf{u} \in \mathcal{A}_\varepsilon$  of  $\mathcal{E}[\cdot]$ . More specifically, they let

$$\mathcal{A} \equiv \{ \mathbf{v} : W^{1,2}(\mathcal{B}) \rightarrow \mathbb{R}^2 \mid \mathbf{v} = \mathbf{0} \text{ almost everywhere on } \partial_1\mathcal{B} \}, \tag{4}$$

and obtain the first variation of  $\mathcal{E}[\cdot]$  at  $\mathbf{u}$  in the form

$$\langle D\mathcal{E}[\mathbf{u}], \mathbf{v} \rangle \equiv a[\mathbf{u}, \mathbf{v}] - f[\mathbf{v}], \quad \forall \mathbf{v} \in \mathcal{A},$$

where  $a[\cdot, \cdot]$  and  $f[\cdot]$  are defined in (2). It is then shown that there exists a scalar Lagrange multiplier field  $\lambda : \mathcal{L}^2(\mathcal{B}) \rightarrow \mathbb{R}$  such that the first variation has the equivalent representation

$$\langle D\mathcal{E}[\mathbf{u}], \mathbf{v} \rangle = \int_{\mathcal{B}} \lambda \operatorname{cof} \nabla\mathbf{f} \cdot \nabla\mathbf{v} d\mathbf{x},$$

for all  $\mathbf{v} \in \mathcal{A}$ , where  $\operatorname{cof} \nabla\mathbf{f}$  is the cofactor of the deformation gradient and we recall from above that  $\mathbf{f}(\mathbf{x}) = \mathbf{x} + \mathbf{u}(\mathbf{x})$ . Then, defining

$$\mathcal{B}_> \equiv \operatorname{int}[\{ \mathbf{x} \in \mathcal{B} : \det \nabla\mathbf{f} > \varepsilon \}], \quad \mathcal{B}_= \equiv \operatorname{int}[\{ \mathbf{x} \in \mathcal{B} : \det \nabla\mathbf{f} = \varepsilon \}], \tag{5}$$

where  $\operatorname{int}[\cdot]$  denotes the interior of a set, the necessary first variation conditions for the existence of a minimizer were shown to be given by:

- The Euler–Lagrange equations

$$\operatorname{Div} \mathbf{T} + \mathbf{b} = \mathbf{0} \quad \text{in } \mathcal{B}_>, \quad \operatorname{Div}(\mathbf{T} - \varepsilon\lambda(\nabla\mathbf{f})^{-T}) + \mathbf{b} = \mathbf{0}, \quad \lambda \geq 0, \quad \text{in } \mathcal{B}_=, \tag{6}$$

together with the boundary conditions

$$\mathbf{T}\mathbf{n} = \bar{\mathbf{t}} \quad \text{on } \partial\mathcal{B}_> \cap \partial_2\mathcal{B}, \quad (\mathbf{T} - \varepsilon\lambda(\nabla\mathbf{f})^{-T})\mathbf{n} = \bar{\mathbf{t}}, \quad \text{on } \partial\mathcal{B}_= \cap \partial_2\mathcal{B}, \tag{7}$$

where  $\mathbf{T} = \mathbb{C}[\mathbf{E}]$  is the constitutive stress tensor and  $\mathbf{n}$  is the outer unit normal to  $\partial_2\mathcal{B}$ .

- Jump conditions across  $\Sigma \equiv \bar{\mathcal{B}}_> \cap \bar{\mathcal{B}}_=$ , which is assumed to be sufficiently smooth,

$$(\mathbf{T} - \varepsilon\lambda(\nabla\mathbf{f})^{-T})\Big|_{\Sigma \cap \bar{\mathcal{B}}_=} \mathbf{n} = \mathbf{T}\Big|_{\Sigma \cap \bar{\mathcal{B}}_>} \mathbf{n}, \tag{8}$$

where  $\mathbf{n}$  is a unit normal to  $\Sigma$  and where  $\Sigma \cap \bar{\mathcal{B}}_=$  and  $\Sigma \cap \bar{\mathcal{B}}_>$  mean that the evaluations are understood as limits to the dividing interface  $\Sigma$  from within  $\mathcal{B}_=$  and  $\mathcal{B}_>$ , respectively.

The expression  $\mathbf{T} - \varepsilon\lambda(\nabla\mathbf{f})^{-T}$  is regarded as the total stress in  $\mathcal{B}_=$ , with  $\lambda$  representing the *constraint stress*.

An *interior penalty functional formulation* of the minimization problem (1)–(3) consists of replacing the energy functional (1)b by a penalized potential energy functional  $\mathcal{E}_\gamma : \mathcal{A}_\varepsilon \rightarrow \bar{\mathbb{R}}$ ,  $\bar{\mathbb{R}} \equiv \mathbb{R} \cup \{\infty\}$ , of the form

$$\mathcal{E}_\gamma[\mathbf{u}] = \mathcal{E}[\mathbf{u}] + \frac{1}{\gamma} \mathcal{Q}[\mathbf{u}], \tag{9}$$

where  $\gamma > 0$  is a penalty parameter and  $\mathcal{Q} : \mathcal{A}_\varepsilon \rightarrow \bar{\mathbb{R}}$  is an *interior penalty functional*, also called a *barrier functional*. The penalty functional is designed so that minimizers of  $\mathcal{E}_\gamma[\cdot]$  lie in the interior of the constraint set  $\mathcal{A}_\varepsilon$ . Thus, the addition of  $(1/\gamma)\mathcal{Q}$  has the effect of establishing a barrier on the boundary of the constraint set  $\mathcal{A}_\varepsilon$  that prevents a search procedure for a minimizer from leaving the set  $\mathcal{A}_\varepsilon$ . In this work, we consider the barrier functional defined by

$$\mathcal{Q}[\mathbf{v}] = \int_{\mathcal{B}} \frac{1}{\det(\mathbf{1} + \nabla\mathbf{v}) - \varepsilon} \, d\mathbf{x}, \quad \forall \mathbf{v} \in \mathcal{A}_\varepsilon. \tag{10}$$

Observe from (10) that  $\mathcal{Q}$  is nonnegative on  $\mathcal{A}_\varepsilon$  and satisfies  $\mathcal{Q}[\mathbf{v}] \rightarrow \infty$  as  $\mathbf{v}$  approaches the boundary of  $\mathcal{A}_\varepsilon$ .

We then wish to find an admissible displacement field  $\mathbf{u}_\gamma \in \mathcal{A}_\varepsilon$  that minimizes the penalized potential  $\mathcal{E}_\gamma[\cdot]$ , that is,

$$\min_{\mathbf{v} \in \mathcal{A}_\varepsilon} \mathcal{E}_\gamma[\mathbf{v}], \tag{11}$$

where  $\mathcal{E}_\gamma[\mathbf{v}]$  is given by the expressions (9), (1)b, (2), and (10). This is a constrained problem, and indeed the functional to be minimized is somewhat more complicated than the original energy functional (1)b. The advantage of considering this problem, however, is that we can use numerical procedures commonly employed in the numerical approximation of solutions of unconstrained problems.

On the other hand, an *exterior penalty functional formulation* of the minimization problem (1)–(3) consists of replacing the energy functional (1)b by a penalized potential energy functional  $\mathcal{E}_\delta : \mathcal{A} \rightarrow \mathbb{R}$  of the form

$$\mathcal{E}_\delta[\mathbf{u}] = \mathcal{E}[\mathbf{u}] + \frac{1}{\delta} \mathcal{P}[\mathbf{u}], \tag{12}$$

where  $\delta > 0$  is a penalty parameter and  $\mathcal{P} : \mathcal{A} \rightarrow \mathbb{R}$  is a *penalty functional*, which is nonnegative in  $\mathcal{A}$  and is designed so that  $\mathcal{P}[\mathbf{v}]$  increases with the distance from  $\mathbf{v}$  to the constraint set  $\mathcal{A}_\varepsilon$ . In this work, we

consider

$$\mathcal{P}[\mathbf{v}] = \frac{1}{2} \int_B \left[ \max(0, -p(\mathbf{v})) \right]^2 d\mathbf{x}, \quad \forall \mathbf{v} \in \mathcal{A}, \tag{13}$$

where  $\max(0, -p) \equiv (-p + |p|)/2$  and

$$p(\mathbf{v}) = \det(\mathbf{1} + \nabla \mathbf{v}) - \varepsilon. \tag{14}$$

Clearly,  $\mathcal{P}[\mathbf{v}] = 0$  if the injectivity constraint is satisfied; otherwise,  $\mathcal{P}[\mathbf{v}] > 0$ . In Section 4 we see that the choice (13) for  $\mathcal{P}$  leads to a discrete version of the penalized energy functional  $\mathcal{E}_\delta$  that is continuous and differentiable everywhere.

We then wish to find an admissible displacement field  $\mathbf{u}_\delta \in \mathcal{A}$  that minimizes the penalized potential  $\mathcal{E}_\delta[\cdot]$ , that is,

$$\min_{\mathbf{v} \in \mathcal{A}} \mathcal{E}_\delta[\mathbf{v}], \tag{15}$$

where  $\mathcal{E}_\delta[\mathbf{v}]$  is given by (12), (1)b, (2), (13), and (14). This is an unconstrained problem, which has the advantage of yielding discrete minimization problems that can be solved by classical unconstrained optimization techniques.

In Section 4 we use both penalty formulations presented above to construct a numerical scheme that is used in Section 5 for the solution of the constrained plane problem presented in Section 3.2.

### 3. The pipe problem

In this section we present the solution of a plane problem, which will serve as a model problem in our computations, in the context of both the classical linear theory, Section 3.1, and the constrained minimization theory, Section 3.2.

**3.1. The unconstrained pipe problem.** In classical linear elasticity, the *pipe problem* concerns the equilibrium of a homogeneous and aeolotropic plate of uniform thickness whose cross section is bounded by two concentric circles, that is, a pipe whose length is the thickness of the plate with an inner radius  $\rho_i$  and an outer radius  $\rho_e$ . The pipe is radially compressed along its external contour by a uniformly distributed normal pressure  $p$  and is subjected to a normal force  $Q$  acting on its flat ends. In isotropic elasticity,  $Q = 0$  characterizes a state of generalized plane stress parallel to the flat ends of a thin plate. In general, however, this is not the case, that is, we may have  $Q = 0$  and still have nonzero normal stresses acting on the flat ends that cannot be disregarded. We comment more on this below.

In a cylindrical coordinate system  $(\rho, \theta, \zeta)$ , we employ the contracted notation  $\sigma_\alpha$ ,  $\alpha = 1, 2, \dots, 6$ , for the stress components, where  $\sigma_1 = \sigma_{\rho\rho}$ ,  $\sigma_2 = \sigma_{\theta\theta}$ ,  $\sigma_3 = \sigma_{\zeta\zeta}$ ,  $\sigma_4 = \sigma_{\theta\zeta}$ ,  $\sigma_5 = \sigma_{\zeta\rho}$ ,  $\sigma_6 = \sigma_{\rho\theta}$ . An analogous notation is also employed for the strain components, that is,  $\epsilon_1 = \epsilon_{\rho\rho}$ ,  $\epsilon_2 = \epsilon_{\theta\theta}$ ,  $\epsilon_3 = \epsilon_{\zeta\zeta}$ ,  $\epsilon_4 = 2\epsilon_{\theta\zeta}$ ,  $\epsilon_5 = 2\epsilon_{\zeta\rho}$ ,  $\epsilon_6 = 2\epsilon_{\rho\theta}$ . These components are related to each other by the linear constitutive relations

$$\sigma_\alpha = c_{\alpha\beta} \epsilon_\beta, \tag{16}$$

where  $c_{\alpha\beta}$  are the elastic constants for a cylindrically aeolotropic material. The corresponding  $6 \times 6$  matrix,  $[c_{\alpha\beta}]$ , is symmetric and positive definite. In this work, we consider that  $c_{\alpha\beta} = 0$  for  $\alpha \leq 3$ ,  $\beta > 3$  and for  $\beta > \alpha > 3$ . Following Christensen [1994], we call the corresponding material *cylindrically orthotropic*.

We assume that the stress components are radially symmetric with respect to the center of the pipe, so that  $\sigma_\alpha = \sigma_\alpha(\rho)$ . In the absence of body force, the equilibrium equations for the pipe problem require that  $\sigma_5 = \sigma_6 = 0$  and yield the equation

$$\frac{\partial \sigma_1}{\partial \rho} + \frac{(\sigma_1 - \sigma_2)}{\rho} = 0.$$

This equation is identically satisfied by the introduction of a stress function  $\phi : \mathbb{R} \rightarrow \mathbb{R}$  that is related to the stress components  $\sigma_i, i = 1, 2$ , through the expressions

$$\sigma_1 = \frac{\phi'(\rho)}{\rho}, \quad \sigma_2 = \phi''(\rho), \tag{17}$$

where  $(\cdot)' \equiv d(\cdot)/d\rho$ .

On the other hand, we can invert the constitutive relations (16) to obtain the strain-stress relations

$$\epsilon_\alpha = s_{\alpha\beta}\sigma_\beta, \tag{18}$$

where  $s_{\alpha\beta}$  are the elastic compliances of the cylindrically aeolotropic material. Since  $\sigma_5 = \sigma_6 = 0$ , we have that  $\epsilon_5 = \epsilon_6 = 0$  for a cylindrically orthotropic material. Also, it follows from both (17) and (18) that  $\epsilon_\alpha = \epsilon_\alpha(\rho), \alpha = 1, 2$ . The compatibility conditions for the pipe problem are then satisfied if

$$\frac{\partial(\rho\epsilon_2)}{\partial \rho} - \epsilon_1 = 0, \tag{19}$$

$\epsilon_3$  is constant, and  $\epsilon_4 = 0$ .

To solve the differential equation (19), first, we use the strain-stress relations (18) to obtain

$$\sigma_3 = \frac{1}{s_{33}}(-s_{31}\sigma_1 - s_{32}\sigma_2 + \epsilon_3). \tag{20}$$

We then substitute (17) and (20) into (18) to find that

$$\epsilon_\alpha = \frac{1}{s_{33}} \left( s_{\alpha 313} \frac{\phi'(\rho)}{\rho} + s_{\alpha 323} \phi''(\rho) + s_{\alpha 3} \epsilon_3 \right), \quad \alpha = 1, 2, \tag{21}$$

where

$$s_{\alpha 3\beta 3} \equiv s_{\alpha\beta} s_{33} - s_{3\alpha} s_{3\beta}, \quad \alpha, \beta = 1, 2, \tag{22}$$

is the determinant of a minor submatrix of the matrix  $\hat{S} \equiv [s_{\delta\gamma}]$  for  $\delta, \gamma = 1, 2, 3$ . Substituting (21) into (19), we find that

$$\frac{d}{d\rho}(\rho\phi''(\rho)) - \kappa^2 \frac{\phi'(\rho)}{\rho} = \left( \frac{s_{13} - s_{23}}{s_{2323}} \right) \epsilon_3, \quad \kappa \equiv \sqrt{\frac{s_{1313}}{s_{2323}}}, \tag{23}$$

where we have used the fact that  $s_{\alpha 3\alpha 3}$ , no sum on  $\alpha$ , is positive since it is the determinant of a principal submatrix of  $\hat{S}$ .

$$c_{11} = \frac{s_{2323}}{\det \hat{S}}, \quad c_{22} = \frac{s_{1313}}{\det \hat{S}}, \quad c_{12} = -\frac{s_{1323}}{\det \hat{S}}. \tag{24}$$

Observe from (23)b together with (24) that  $\kappa$  is also given by

$$\kappa = \sqrt{\frac{c_{22}}{c_{11}}}. \tag{25}$$

The general solution of the differential equation (23) is given by

$$\phi(\rho) = \frac{\alpha^+}{1+\kappa} \rho^{(1+\kappa)} + \frac{\alpha^-}{1-\kappa} \rho^{(1-\kappa)} + \frac{\tilde{\epsilon}_3}{2} \rho^2 + \hat{\phi}, \quad \tilde{\epsilon}_3 \equiv \left( \frac{s_{13} - s_{23}}{s_{2323} - s_{1313}} \right) \epsilon_3, \tag{26}$$

where  $\hat{\phi}$  is a constant of integration. Using (26), we obtain from both (17) and (20) that

$$\begin{aligned} \sigma_1 &= \alpha^+ \rho^{(-1+\kappa)} + \alpha^- \rho^{-(1+\kappa)} + \tilde{\epsilon}_3, \\ \sigma_2 &= \kappa \alpha^+ \rho^{(-1+\kappa)} - \kappa \alpha^- \rho^{-(1+\kappa)} + \tilde{\epsilon}_3, \\ \sigma_3 &= -\frac{s_{13} + \kappa s_{23}}{s_{33}} \alpha^+ \rho^{(-1+\kappa)} - \frac{s_{13} - \kappa s_{23}}{s_{33}} \alpha^- \rho^{-(1+\kappa)} + \left( \frac{s_{22} - s_{11}}{s_{2323} - s_{1313}} \right) \epsilon_3. \end{aligned} \tag{27}$$

Notice from (27)c that  $\sigma_{33}$  depends on  $\rho$ , a fact observed by Tings [1999], and, in general, cannot be disregarded, as was done by Lekhnitskii [1968, Page 52], even when the pipe has small axial length, that is, it is *disk-like*. This means that no generalized plane stress parallel to the flat ends of the pipe is possible for a radially symmetric distribution of stress in a cylindrically orthotropic body. We can, however, integrate (27)c over a flat end of the pipe and obtain  $Q$ , the resultant force on that end. As observed by Tings [1999], we can allow free extension of the pipe in the axial direction in the sense that  $Q = 0$ , which yields an expression for the determination of the constant  $\epsilon_3$ .

The plane stress analysis carried out by Lekhnitskii [1968], which disregards  $\sigma_3$ , is still valid for particular classes of cylindrically aeolotropic materials, which include the isotropic materials and materials for which  $s_{13} = s_{23} = 0$ . In this last case, observe from (27)c together with (22) that we must have  $\epsilon_3 = 0$ .

Now, recalling that the strains depend only on  $\rho$  and disregarding rigid body displacements, we have that the displacement field  $\mathbf{u}$  is of the form  $\mathbf{u} = u(\rho)\mathbf{e}_\rho + \epsilon_3\mathbf{e}_z$ , where  $(\mathbf{e}_\rho, \mathbf{e}_\theta, \mathbf{e}_z)$  is an orthonormal basis for the cylindrical coordinate system. It then follows from the linear strain-displacement relations

$$\epsilon_1 = u'(\rho), \quad \epsilon_2 = \frac{u(\rho)}{\rho}, \tag{28}$$

together with (21) and (27), that

$$u(\rho) = \hat{\alpha}^+ \rho^\kappa + \hat{\alpha}^- \rho^{-\kappa} + \hat{\epsilon}_3 \rho, \tag{29}$$

where

$$\begin{aligned} \hat{\alpha}^+ &\equiv \left( \frac{s_{2313} + \kappa s_{2323}}{s_{33}} \right) \alpha^+, & \hat{\alpha}^- &\equiv \left( \frac{s_{2313} - \kappa s_{2323}}{s_{33}} \right) \alpha^-, \\ \hat{\epsilon}_3 &\equiv \left[ \frac{(s_{2313} + s_{2323})s_{13} - (s_{2313} + s_{1313})s_{23}}{(s_{2323} - s_{1313})s_{33}} \right] \epsilon_3. \end{aligned} \tag{30}$$

Of major interest in this work is the sign of the Jacobian determinant of the deformation field  $\mathbf{f} \equiv \mathbf{x} + \mathbf{u}$ , given by

$$J \equiv \det \nabla \mathbf{f} = (1 + \epsilon_1)(1 + \epsilon_2)(1 + \epsilon_3). \tag{31}$$

Because  $\epsilon_3$  is constant and small compared to unity, it is of no major consequence to consider only the case  $\epsilon_3 = 0$  in this work, which is equivalent to assuming that the pipe is in a state of *plane strain* parallel to its flat ends.

By imposing the condition of zero displacement on the inner radius,  $u(\rho_i) = 0$ , and the pressure condition on the outer radius,  $\sigma_{\rho\rho}(\rho_e) = -p$ , we find that

$$\alpha^+ = (s_{2313} - \kappa s_{2323})\rho_i^{-\kappa}\rho_e p/\hat{\alpha}, \quad \alpha^- = -(s_{2313} + \kappa s_{2323})\rho_i^\kappa\rho_e p/\hat{\alpha}, \quad (32)$$

where

$$\hat{\alpha} \equiv (s_{2313} + \kappa s_{2323})\left(\frac{\rho_i}{\rho_e}\right)^\kappa - (s_{2313} - \kappa s_{2323})\left(\frac{\rho_i}{\rho_e}\right)^{-\kappa}. \quad (33)$$

Observe from both expressions (22) and (23)b that  $s_{2313}^2 - \kappa^2 s_{2323}^2 = s_{2313}^2 - s_{1313}s_{2323} = -s_{33} \det \hat{S} < 0$ . We then have both  $\kappa s_{2323} - s_{2313} > 0$  and  $\kappa s_{2323} + s_{2313} > 0$ , and it follows from (33) that  $\hat{\alpha} > 0$ .

Substituting (30)a, (32), (33), and (24) into (29), we obtain

$$u(\rho) = -\frac{\rho_i}{2\kappa} \left[ \left(\frac{\rho}{\rho_i}\right)^\kappa - \left(\frac{\rho}{\rho_i}\right)^{-\kappa} \right] \frac{\hat{p}}{p_1}, \quad \hat{p} \equiv \frac{p}{c_{11}}, \quad \rho_i < \rho < \rho_e, \quad (34)$$

where

$$p_1 = \frac{\rho_i}{2\kappa\rho_e} \left[ (\kappa - \mu_\theta) \left(\frac{\rho_i}{\rho_e}\right)^\kappa + (\kappa + \mu_\theta) \left(\frac{\rho_i}{\rho_e}\right)^{-\kappa} \right] > 0, \quad \mu_\theta \equiv \frac{c_{12}}{c_{11}}. \quad (35)$$

In the limit, as  $\rho_i \rightarrow 0$ , we obtain from (34) together with (35) the Lekhnitskii classical solution for the *disk problem*, which is given by

$$u_0(\rho) \equiv -\left(\frac{\rho}{\rho_e}\right)^\kappa \rho_e q, \quad q \equiv \frac{p}{\sqrt{c_{11}c_{22}} + c_{12}}, \quad 0 < \rho < \rho_e, \quad (36)$$

The expression (36) is presented by Fosdick and Royer-Carfagni [2001, Equation 1.18] in a slightly different notation.

The disk problem is also considered by Tarn [2002] as a special case of a class of generalized plane problems. The author is mainly concerned with the issue of stress singularity at the center of the disk that results from (27) when  $0 < \kappa < 1$ . He attributes this singular behavior to a conflicting definition of anisotropy at  $\rho = 0$ . To resolve this, he considers plane problems involving two concentric cylinders of different elastic materials. The outer cylinder is cylindrically anisotropic and the inner solid cylinder is transversely isotropic. Even though the stress fields obtained from the solutions of these problems are not singular at the center of the resulting compound cylinder, it is observed by Fosdick et al. [2008] that self-intersection is still an issue in his work.

Here, we return to the case  $\rho_i > 0$ , which corresponds to a compound cylinder with a rigid core, and perform a detailed analysis of the solution (34). For this, we take the derivative of (34) with respect to  $\rho$  and obtain

$$u'(\rho) = -\frac{1}{2} \left[ \left(\frac{\rho}{\rho_i}\right)^{\kappa-1} + \left(\frac{\rho}{\rho_i}\right)^{-(\kappa+1)} \right] \frac{\hat{p}}{p_1}, \quad (37)$$

which is negative in the interval  $(\rho_i, \rho_e)$ . Another derivative of (34) shows that  $u''(\rho) > 0$  for  $0 < \kappa < 1$ , which means that  $u$  is a convex function of  $\rho$  and that  $u'$  is a monotonically increasing function of  $\rho$  with its minimum at  $\rho = \rho_i$ . Thus, a critical value of  $\hat{p}$  that yields  $J = 0$  at  $\rho = \rho_i$  in (31) and (28)a is obtained from  $u'(\rho_i) = -1$  in (37) and is given by  $\hat{p} = p_1$ , where  $p_1$  is defined by (35)a. For larger

values of  $\hat{\rho}$ ,  $J = 0$  for a unique radius greater than  $\rho_i$ . Clearly, we may have  $p_1$ , and hence  $\hat{\rho}$ , as small as we wish by decreasing the value of  $\rho_i$  and still have bounded stresses and strains everywhere. In this work, we are only concerned with  $0 < \kappa < 1$ .

Similarly, we can show that  $u(\rho)/\rho$  is convex at  $\rho = \rho_i$ . We can also show that  $u(\rho)/\rho$  has a unique minimum at a point with radius  $\hat{\rho} > \rho_i$  for  $0 < \kappa < 1$ . This minimum reaches the value  $-1$ , which corresponds to  $J = 0$  from (31) together with (28)b, for  $\hat{\rho} = p_2$ , where

$$p_2 = (1 - \kappa) \left( \frac{1 + \kappa}{1 - \kappa} \right)^{(1+\kappa)/2\kappa} p_1. \tag{38}$$

This critical value of  $\hat{\rho}$  is greater than  $p_1$  for  $0 < \kappa < 1$ . In fact, observe from Figure 1 that  $p_2 > 2p_1$ .

To avoid crushing of the outer surface into the inner surface of the pipe, the displacement  $u(\rho_e)$  must be such that  $-u(\rho_e)/\rho_e < 1 - \rho_i/\rho_e$ , which, because of (34), imposes the restriction

$$\hat{\rho} < p_c \equiv \frac{2(1 - \eta)\eta^{\kappa-1}}{1 - \eta^{2\kappa}} p_1, \quad \eta \equiv \rho_i/\rho_e. \tag{39}$$

Since  $p_c \gg p_1$  for both  $\rho_i \ll \rho_e$  and  $\kappa < 1$ , we conclude from above that local injectivity is lost for nonzero values of  $\hat{\rho}$  that are small compared to the critical value  $p_c$  for which global injectivity is lost.

Using (31) with  $\epsilon_3 = 0$  and (28), (34), and (37), we obtain the expression

$$J = \left\{ 1 - \frac{1}{2} \left[ \left( \frac{\rho}{\rho_i} \right)^{\kappa-1} + \left( \frac{\rho}{\rho_i} \right)^{-(\kappa+1)} \right] \frac{\hat{\rho}}{p_1} \right\} \left\{ 1 - \frac{1}{2\kappa} \left[ \left( \frac{\rho}{\rho_i} \right)^{\kappa-1} - \left( \frac{\rho}{\rho_i} \right)^{-(\kappa+1)} \right] \frac{\hat{\rho}}{p_1} \right\}. \tag{40}$$

We then see from (40) together with the previous discussion on the critical values for  $\hat{\rho}$  that, as  $\hat{\rho}$  increases from zero,  $J$  is positive in  $[\rho_i, \rho_e]$  for  $\hat{\rho} < p_1$ . For  $p_1 \leq \hat{\rho} \leq p_2$ ,  $J$  is nonpositive in  $[\rho_i, \rho_1]$ , where  $u'(\rho_1) = -1$ . In particular,  $J = 0$  at  $\rho = \rho_1$ . If  $\hat{\rho} = p_2$ , we also have that  $J = 0$  at  $\rho = \hat{\rho}$ , where we recall from above that  $\hat{\rho}$  is the radius at which  $u(\rho)/\rho$  attains its minimum. For  $p_2 < \hat{\rho} < p_c$ ,  $u(\hat{\rho})/\hat{\rho} < -1$  and we have two roots  $\rho_A$  and  $\rho_B$ , with  $\rho_A < \rho_B$ , for the algebraic equation  $u(\rho)/\rho = -1$ . Since  $u(\rho_e)/\rho_e > -1 + \rho_i/\rho_e$ , both roots belong to the interval  $(\rho_i, \rho_e)$  and are such that  $u(\rho)/\rho \leq -1$  in the interval  $[\rho_A, \rho_B]$ . Outside this interval,  $u(\rho)/\rho > -1$ . Thus, we have  $J = 0$  at  $\rho = \rho_1, \rho_A$ , and  $\rho_B$ . In Section 5 we show a numerical example for which  $\rho_i < \rho_A < \rho_1 < \rho_B < \rho_e$ . In this case,  $J$  oscillates;

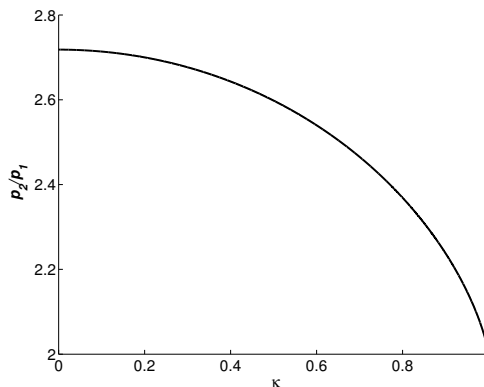


**Figure 1.** The ratio  $p_2/p_1$  versus  $\kappa$ .

it is negative between  $\rho_i$  and  $\rho_A$ , positive between  $\rho_A$  and  $\rho_1$ , negative again between  $\rho_1$  and  $\rho_B$ , and positive again between  $\rho_B$  and  $\rho_e$ .

In the case of  $\rho_i = 0$ ,  $\rho_1 = (\kappa q)^{1/(1-\kappa)}\rho_e$  and  $u(\rho)/\rho$  has only one root given by  $\rho_2 = q^{1/(1-\kappa)}\rho_e$ , where  $q$  is defined by the expression (36)b. Here,  $J < 0$  inside the annular region defined by

$$0 < \kappa q < \left(\frac{\rho}{\rho_e}\right)^{1-\kappa} < q.$$

Outside the annular region, that is, for small and large values of  $(\rho/\rho_e)^{1-\kappa}$ , we have  $J > 0$ . This feature was first noted by Fosdick and Royer-Carfagni [2001].

Thus, for  $0 < \kappa < 1$ , the classical solution has no physical meaning and therefore should be rejected as a viable solution. The anomalous behavior of material overlapping provides, however, motivation to use a pseudolinear theory which respects the constraint that admissible deformations be at least locally invertible, that is, that  $\det \nabla \mathbf{f} > 0$ .

**3.2. The constrained pipe problem.** The solution of the unconstrained pipe problem in Section 3.1 predicts material overlapping for  $\kappa \in (0, 1)$ . In this section, we consider that  $\kappa \in (0, 1)$  and use the first variation conditions (6)–(8) to find a minimizer of (1)–(3) for the constrained pipe problem.

Fosdick and Royer-Carfagni [2001] solve the radially symmetric disk problem of Lekhnitskii outlined in Section 3.1 for the material parameter  $\kappa \in (0, 1)$  within the constrained minimization theory outlined in Section 2. They consider only a radially symmetric type solution and our analysis below follows their approach. Recently, Fosdick et al. [2008] have considered the full two-dimensional disk problem and have presented numerical results which show that this symmetry does not persist for all values of the elastic constant  $c_{66}$  in (16). Because the constrained theory is nonlinear, there are values of  $c_{66}$  for which bifurcation from radial symmetry to nonradial symmetry takes place.

The sets  $\mathcal{B}_=$  and  $\mathcal{B}_>$  of (5), where the constraint of local injectivity is active ( $\det \nabla \mathbf{f} = \varepsilon$ ) and nonactive ( $\det \nabla \mathbf{f} > \varepsilon$ ), respectively, will be determined explicitly as  $\mathcal{B}_= = \{\mathbf{x} = \rho \mathbf{e}_\rho \in \mathcal{B} : \rho_i \leq \rho < \rho_a\}$ ,  $\mathcal{B}_> = \{\mathbf{x} = \rho \mathbf{e}_\rho \in \mathcal{B} : \rho_a < \rho < \rho_e\}$ , for some  $\rho_a \in [\rho_i, \rho_e]$ .

Assuming that the displacement field must be radially symmetric with respect to the center of the pipe in a state of plane strain, that is,  $\mathbf{u} = u(\rho)\mathbf{e}_\rho$ , we observe that (6)–(8) have the following forms:

- The Euler–Lagrange equations:

$$\begin{aligned} u'' + \frac{u'}{\rho} - \kappa^2 \frac{u}{\rho^2} - \left(1 + \frac{u}{\rho}\right) \frac{d\hat{\lambda}}{d\rho} &= 0, & \hat{\lambda} \geq 0, & \text{for } \rho \in (\rho_i, \rho_a), \\ u'' + \frac{u'}{\rho} - \kappa^2 \frac{u}{\rho^2} &= 0 & & \text{for } \rho \in (\rho_a, \rho_e), \end{aligned} \tag{41}$$

where  $\hat{\lambda} \equiv \lambda/c_{11}$ .

- The displacement and traction conditions:

$$u(\rho_i) = 0, \quad u'(\rho_e) + \mu_\theta \frac{u(\rho_e)}{\rho_e} = -\hat{p}, \tag{42}$$

where  $\hat{p}$  is defined by (34)b and  $\mu_\theta$  is defined by (35)b.

- The continuity and jump conditions across  $\rho = \rho_a$ :

$$\begin{aligned} u(\rho_a^+) &= u(\rho_a^-), \\ u'(\rho_a^+) &= u'(\rho_a^-) - \left[ 1 + \frac{u(\rho_a^-)}{\rho_a} \right] \hat{\lambda}(\rho_a^-), \end{aligned} \tag{43}$$

where  $\rho_a^\pm \equiv \lim_{\tau \rightarrow 0}(\rho_a \pm \tau)$  for  $\tau > 0$ . The condition (43)b is obtained from

$$\sigma_{\rho\rho}(\rho_a^+) = \sigma_{\rho\rho}(\rho_a^-) - \left[ 1 + \frac{u(\rho_a^-)}{\rho_a} \right] \hat{\lambda}(\rho_a^-),$$

together with (16), (28), and (43)a. Observe from (43)b that the jump in  $u'$  is zero at  $\rho = \rho_a$  provided that  $\hat{\lambda}(\rho_a^-) = 0$ . We show below that this is indeed the case.

The imposition of the injectivity constraint  $\det(\mathbf{1} + \nabla \mathbf{u}) = \varepsilon > 0$  in  $(\rho_i, \rho_a)$  yields the problem of finding  $u : (\rho_i, \rho_a) \rightarrow \mathbb{R}$  that satisfies

$$\frac{1}{2\rho} \frac{d}{d\rho}(\rho + u)^2 = \varepsilon \quad \text{in } (\rho_i, \rho_a), \quad u(\rho_i) = 0.$$

The solution of this problem is

$$u(\rho) = g(\rho) - \rho, \quad g(\rho) = \sqrt{(\rho^2 - \rho_i^2)\varepsilon + \rho_i^2}, \quad \text{for } \rho \in (\rho_i, \rho_a). \tag{44}$$

Substituting the expression (44) into the first Euler–Lagrange equation (41)a, we obtain a first-order differential equation for  $\hat{\lambda}$ . The solution of this equation is given by

$$\hat{\lambda}(\rho) = -\frac{(1 - \varepsilon)\rho_i^2}{2} \left[ \frac{1}{g(\rho)^2} - \frac{1}{g(\tilde{\rho})^2} \right] + \log\left(\frac{g(\rho)}{g(\tilde{\rho})}\right) - \kappa^2 \log\left(\frac{\rho}{\tilde{\rho}}\right) - \frac{(1 - \kappa^2)}{\sqrt{\varepsilon}} \log\left(\frac{\sqrt{\varepsilon}\rho + g(\rho)}{\sqrt{\varepsilon}\tilde{\rho} + g(\tilde{\rho})}\right), \tag{45}$$

where  $g(\rho)$  is given by (44)b and  $\tilde{\rho} \in \mathbb{R}$  is to be determined consistent with  $\hat{\lambda}(\tilde{\rho}) \geq 0$ . We show in the Appendix that  $u'(\rho_a^+) = u'(\rho_a^-)$  and that  $\tilde{\rho} = \rho_a$ .

The general solution of the second Euler–Lagrange equation (41)b is of the form

$$u(\rho) = \beta^+ \rho^\kappa + \beta^- \rho^{-\kappa}, \tag{46}$$

where both constants  $\beta^+$  and  $\beta^-$  are determined from the continuity and jump conditions (43). These constants are given by

$$\beta^+ = \frac{\rho_a^{-\kappa+1}}{2\kappa} \left[ -(1 + \kappa) + \kappa \frac{g(\rho_a)}{\rho_a} + \frac{\varepsilon\rho_a}{g(\rho_a)} \right], \quad \beta^- = \frac{\rho_a^{\kappa+1}}{2\kappa} \left[ 1 - \kappa + \kappa \frac{g(\rho_a)}{\rho_a} - \frac{\varepsilon\rho_a}{g(\rho_a)} \right]. \tag{47}$$

We still need to find  $\rho_a$  in (47). For this, we substitute (46) and (47) into the traction condition (42)b and obtain the algebraic equation

$$0 = r(\zeta) \equiv s(\zeta; \kappa) + s(\zeta; -\kappa) + \hat{p}, \quad \zeta \equiv \frac{\rho_a}{\rho_e}, \tag{48}$$

where

$$s(\zeta; \kappa) \equiv \left( \frac{\kappa + \mu_\theta}{2\kappa} \right) \zeta^{1-\kappa} \left[ -(1 + \kappa) + \frac{\kappa \hat{g}(\zeta)}{\zeta} + \frac{\varepsilon\zeta}{\hat{g}(\zeta)} \right], \tag{49}$$

is a function of  $\zeta$  parameterized by  $\kappa$  and

$$\hat{g}(\zeta) \equiv \sqrt{\varepsilon\zeta^2 + (1 - \varepsilon)\zeta_i^2}, \quad \zeta_i \equiv \frac{\rho_i}{\rho_e}. \tag{50}$$

First, notice from the expressions (48)–(50) that  $r(\zeta_i) = \hat{p} - (1 - \varepsilon)p_1$ , where  $p_1$  is given by (35)a. Notice also that  $r(1) = \hat{p} - p_0$ , where

$$p_0 \equiv 1 + \mu_\theta - \left[ \frac{\varepsilon + \mu_\theta \hat{g}(1)^2}{\hat{g}(1)} \right] > p_1, \tag{51}$$

since both  $\zeta_i$  and  $\varepsilon > 0$  are small. Taking the derivative of  $r$ , we obtain

$$r'(\zeta) = - \left[ \frac{(\kappa + \mu_\theta)\zeta^{-\kappa} + (\kappa - \mu_\theta)\zeta^\kappa}{2\kappa} \right] \left\{ 1 - \kappa^2 + \frac{\kappa^2 \hat{g}(\zeta)}{\zeta} - \frac{\varepsilon\zeta}{\hat{g}(\zeta)} \left[ 2 - \varepsilon \left( \frac{\zeta}{\hat{g}(\zeta)} \right)^2 \right] \right\}, \quad \zeta \in (\zeta_i, 1),$$

which is negative, because  $\kappa + \mu_\theta > 0$ ,  $\kappa - \mu_\theta > 0$ , and  $\varepsilon > 0$  is small. Thus, if  $r(\zeta_i) < 0$ , then  $r(\zeta) = 0$  has no roots, which is consistent with results obtained in Section 3.1, according to which  $\hat{p} - p_1 < 0$  implies no self-intersection. If, on the other hand, both  $r(\zeta_i) \geq 0$  and  $\hat{p} \leq p_0$ , then there exists a unique  $\zeta \in [0, 1]$  that satisfies  $r(\zeta) = 0$ . In particular, if  $\hat{p} = (1 - \varepsilon)p_1$ , then  $\zeta = \zeta_i$  and if  $\hat{p} = p_0$ , then  $\zeta = 1$ . Furthermore, if  $\hat{p} > p_0$ , no  $\zeta \in [0, 1]$  exists that satisfies  $r(\zeta) = 0$ . In this case,  $\rho_a = \rho_e$ , which means that the constraint is active in the whole pipe.

In the limit, as  $\rho_i \rightarrow 0$  in (44)b, we obtain the solution of the *constrained disk problem* considered by Fosdick and Royer-Carfagni [2001], which is given by

$$u(\rho) = \begin{cases} -(1 - \sqrt{\varepsilon})\rho & \text{for } \rho \in (0, \rho_a), \\ -\frac{(1 - \sqrt{\varepsilon})\rho_a}{2\kappa} \left[ (1 + \kappa) \left( \frac{\rho}{\rho_a} \right)^\kappa - (1 - \kappa) \left( \frac{\rho}{\rho_a} \right)^{-\kappa} \right] & \text{for } \rho \in (\rho_a, \rho_e). \end{cases} \tag{52}$$

The radius  $\rho_a$  in (52) is determined from an algebraic equation obtained from (48)–(50) when  $\rho_i = 0$ . Fosdick and Royer-Carfagni [2001] show that there exists a unique root for this equation for any positive value of  $p \leq (1 - \sqrt{\varepsilon})(c_{11} + c_{12})$ . If  $p > (1 - \sqrt{\varepsilon})(c_{11} + c_{12})$ , the algebraic equation has no root and  $\rho_a = \rho_e$ . Thus, for any  $p > 0$ , we have a disk-like region of radius  $\rho_a > 0$  where the constraint  $J \equiv \det(\mathbf{1} + \nabla \mathbf{u}) = \varepsilon$  is satisfied.

In the pipe problem, for which  $\rho_i > 0$ , we must have  $p \geq (1 - \varepsilon)p_1$  for the constraint  $J = \varepsilon$  to be satisfied in a region bounded by the radii  $\rho_i$  and  $\rho_a$ . Observe from (35) that  $p_1$  is small for small values of  $\rho_i$ . Also, recall from (51) that  $p_0 > p_1$ . In Section 5 we consider  $(1 - \varepsilon)c_{11}p_1 < p < c_{11}p_0$  and find numerically a root  $\rho_a \in (\rho_i, \rho_e)$  for the algebraic equation (48). Notice that for small  $\varepsilon > 0$  and small  $\zeta_i > 0$ , it follows from (51) together with both (35)b and (50) that  $c_{11}p_0$  is approximately equal to  $c_{11} + (1 - \zeta_i)c_{12}$ , which is of the same order of magnitude as  $(1 - \sqrt{\varepsilon})(c_{11} + c_{12})$ , as referenced in the previous paragraph.

Using (46) together with  $\mathbf{f}(\rho) = [\rho + u(\rho)]\mathbf{e}_\rho$ , we can easily obtain an expression for  $\det \nabla \mathbf{f}(\rho)$ , which is positive everywhere in  $[\rho_i, \rho_e]$ . Thus, the solution (46) together with (47) describe the deformation of the pipe, which is both locally and globally injective.

### 4. The discrete formulation

We wish to construct an approximate solution to both penalty minimization problems (11) and (15) for given penalty parameters  $\gamma$  and  $\delta$ , respectively. For this, it is necessary to consider a finite element formulation based on the introduction of discrete minimization problems over a finite-dimensional space  $\mathcal{A}_h \subset \mathcal{A}$ , where the subscript  $h$  denotes a characteristic length of the finite element and  $\mathcal{A}$  is given by (4). These problems can be solved using an unconstrained minimization method with a line search technique.

Holding  $h$  fixed and increasing  $\gamma$  in the interior penalty formulation, the strategy is to first generate a sequence of solutions parameterized by  $\gamma$  for the discrete problems that converges to an approximate solution  $\mathbf{u}_h^i$  of the minimization problem (1)–(3), as  $\gamma \rightarrow \infty$ . The aim is then to refine the finite element mesh by decreasing  $h$  and repeat the process above. In so doing, we shall generate a sequence of solutions  $\mathbf{u}_h^i$  parameterized by  $h$  which converges to the solution  $\mathbf{u}$  of the original minimization problem (1)–(3).

A similar strategy is used to generate a convergent sequence of solutions  $\mathbf{u}_h^e$  for the exterior penalty formulation. Here,  $\mathbf{u}_h^e$  is the limit function of a sequence of solutions parameterized by  $\delta$  as  $\delta$  tends to zero. In Section 5 we show numerical results which indicate that  $\mathbf{u}_h^i = \mathbf{u}_h^e$  for a given  $h$ .

The strategies outlined above are general and apply to problems in any dimension. Here, however, we consider the two-dimensional model problem described in Section 3 with the imposition of the injectivity constraint  $\det(\mathbf{1} + \nabla \mathbf{v}) \geq \varepsilon > 0$ , where  $\mathbf{v} \in \mathcal{A}$ . In fact, since the fully linear theory in Section 3.1 is radially symmetric, we shall consider only the one-dimensional radially symmetric numerical solution here. Because the constrained theory is nonlinear, radial symmetry need not be the sole possibility as is shown in the work of Fosdick et al. [2008]. Here, we let  $\mathbf{v} = v\mathbf{e}_\rho$ , where  $v$  is a scalar function defined on the interval  $(0, \rho_e)$ .

Since the energy potential  $\mathcal{E}[\cdot]$  is given by (1)b and (2), we can write

$$\mathcal{E}[v\mathbf{e}_\rho] = \pi c_{11} \left\{ \int_{\rho_i}^{\rho_e} \left[ (v')^2 \rho + \frac{(\kappa v)^2}{\rho} \right] d\rho + \mu_\theta v(\rho_e)^2 \right\} + 2\pi p v(\rho_e) \rho_e, \tag{53}$$

for the model problem described in Section 3, where  $\kappa$  and  $\mu_\theta$  are given by, respectively, (25) and (35)b. Since  $\det(\mathbf{1} + \nabla(v\mathbf{e}_\rho)) = (1 + v')(1 + v/\rho)$ , the inverse barrier functional, defined by (10), becomes

$$\mathcal{Q}[v\mathbf{e}_\rho] = 2\pi \int_{\rho_i}^{\rho_e} \frac{\rho}{(1 + v')(1 + v/\rho) - \varepsilon} d\rho, \tag{54}$$

and the exterior penalty functional, defined by (13) and (14), becomes

$$\mathcal{P}[v\mathbf{e}_\rho] = \frac{\pi}{4} \int_{\rho_i}^{\rho_e} \left[ -(1 + v')(1 + v/\rho) + \varepsilon + \left| (1 + v')(1 + v/\rho) - \varepsilon \right|^2 \right] \rho d\rho. \tag{55}$$

The penalized potential  $\mathcal{E}_\gamma[\cdot]$  for the interior formulation is then obtained from (9), (53), and (54), while the penalized potential  $\mathcal{E}_\delta[\cdot]$  for the exterior formulation is obtained from (12), (53), and (55). In both cases, because of the assumption of radial symmetry, the discrete formulations are one-dimensional.

Now, let  $\rho_i \equiv \rho_0 < \rho_1 < \rho_2 < \dots < \rho_n \equiv \rho_e$  be a partition of the interval  $\mathcal{I} \equiv (\rho_i, \rho_e)$  into subintervals  $\mathcal{I}_j = (\rho_{j-1}, \rho_j)$  of length  $\Delta\rho_j = \rho_j - \rho_{j-1}$ ,  $j = 1, 2, \dots, n$ . Let also  $\mathcal{A}_h$  be the set of functions  $v\mathbf{e}_\rho$  such that  $v$  is linear over each subinterval  $\mathcal{I}_j$ ,  $v \in C^0(\mathcal{I})$ , and  $v(\rho_i) = 0$ . Clearly,  $\mathcal{A}_h \subset \mathcal{A}$ , where  $\mathcal{A}$  is given by (4).

Next, introduce the piecewise linear basis functions  $\phi_j \mathbf{e}_\rho \in \mathcal{A}_h, j = 1, 2, \dots, n$ , defined by

$$\phi_j(\rho_k) = \delta_{kj}, k, j = 1, 2, \dots, n.$$

Then, a function  $v_h \mathbf{e}_\rho \in \mathcal{A}_h$  has the representation

$$v_h(\rho) = \mathbf{s} \cdot \mathbf{g}(\rho), \quad \rho \in \mathcal{I}, \tag{56}$$

which is the inner product between the vector  $\mathbf{s} \equiv (\eta_1, \eta_2, \dots, \eta_n) \in \mathbb{R}^n$  and the  $n$ -dimensional vector-valued function  $\mathbf{g} \equiv (\phi_1, \phi_2, \dots, \phi_n)$  defined over the interval  $\mathcal{I}$ . The coefficients  $\eta_i$  are given by

$$\eta_k = v_h(\rho_k). \tag{57}$$

Substituting  $v_h$  into (53)–(55), we obtain

$$\mathcal{E}_h(\mathbf{s}) \equiv \frac{\mathcal{E}[(\mathbf{s} \cdot \mathbf{g}) \mathbf{e}_\rho]}{2\pi p \rho_e} = \frac{c_{11}}{2p \rho_e} \left\{ \int_{\rho_i}^{\rho_e} \left[ (\mathbf{s} \cdot \mathbf{g}')^2 \rho + \frac{(\kappa \mathbf{s} \cdot \mathbf{g})^2}{\rho} \right] d\rho + \mu_\theta [\mathbf{s} \cdot \mathbf{g}(\rho_e)]^2 \right\} + \mathbf{s} \cdot \mathbf{g}(\rho_e), \tag{58}$$

$$\mathcal{Q}_h(\mathbf{s}) \equiv \frac{\mathcal{Q}[(\mathbf{s} \cdot \mathbf{g}) \mathbf{e}_\rho]}{2\pi p \rho_e} = \int_{\rho_i}^{\rho_e} \frac{\rho}{[(1 + \mathbf{s} \cdot \mathbf{g}')(1 + \mathbf{s} \cdot \mathbf{g}/\rho) - \varepsilon]} d\rho, \tag{59}$$

$$\mathcal{P}_h(\mathbf{s}) \equiv \frac{\mathcal{P}[(\mathbf{s} \cdot \mathbf{g}) \mathbf{e}_\rho]}{2\pi p \rho_e} = \frac{1}{8} \int_{\rho_i}^{\rho_e} \left[ -(1 + \mathbf{s} \cdot \mathbf{g}')(1 + \mathbf{s} \cdot \mathbf{g}/\rho) + \varepsilon + |(1 + \mathbf{s} \cdot \mathbf{g}')(1 + \mathbf{s} \cdot \mathbf{g}/\rho) - \varepsilon| \right]^2 \rho d\rho, \tag{60}$$

respectively. Observe from (56)–(60) that  $\mathcal{E}_h, \mathcal{Q}_h$ , and  $\mathcal{P}_h$  are scalar functions of an  $n$ -dimensional vector of coefficients  $\eta_k, k = 1, 2, \dots, n$ . Also,  $\mathcal{P}_h$  is a continuous function of  $\mathbf{s}$  with continuous first derivative.

The discrete versions of the penalized potentials  $\mathcal{E}_\gamma[\cdot]$  and  $\mathcal{E}_\delta[\cdot]$  are then defined by

$$\mathcal{F}_\gamma(\mathbf{s}) \equiv \mathcal{E}_h(\mathbf{s}) + \frac{1}{\gamma} \mathcal{Q}_h(\mathbf{s}), \quad \mathcal{F}_\delta(\mathbf{s}) \equiv \mathcal{E}_h(\mathbf{s}) + \frac{1}{\delta} \mathcal{P}_h(\mathbf{s}), \tag{61}$$

respectively, for a fixed  $h$ . In (61), both penalty parameters  $\gamma$  and  $\delta$  have been redefined so that their new values are their old values multiplied by  $p \rho_e$ . The discrete version of the minimization problem (11), applied to the constrained pipe problem of Section 3.2, consists of finding an  $n$ -dimensional vector  $\mathbf{r}_\gamma \equiv \{\chi_{\gamma 1}, \chi_{\gamma 2}, \dots, \chi_{\gamma n}\}$  that minimizes the scalar function  $\mathcal{F}_\gamma$ , given by (61)a, over all vectors  $\mathbf{s}$  in  $\mathbb{R}^n$  that satisfy the injectivity constraint

$$\det(\mathbf{1} + \nabla((\mathbf{s} \cdot \mathbf{g}) \mathbf{e}_\rho)) - \epsilon = (1 + \mathbf{s} \cdot \mathbf{g}')(1 + \mathbf{s} \cdot \mathbf{g}/\rho)^2 - \epsilon \geq 0, \quad 0 \leq \rho \leq \rho_e. \tag{62}$$

A nodal value of the constraint (62) is evaluated at the midpoint of the subinterval immediately to the left of the node under consideration. For the discrete version of the minimization problem (15), we search for  $\mathbf{r}_\delta \equiv \{\chi_{\delta 1}, \chi_{\delta 2}, \dots, \chi_{\delta n}\}$  that minimizes the scalar function  $\mathcal{F}_\delta$ , given by (61)b, over all vectors  $\mathbf{s}$  in  $\mathbb{R}^n$ . Notice from these statements that the discrete version of (11) is a constrained minimization problem while the discrete version of (15) is an unconstrained minimization problem.

The discrete minimization problems stated above are solved iteratively using a standard unconstrained second-order minimization method with a line search technique. The method is based on an *iterative descent algorithm* presented in [Aguiar 2006], which is used here to search for an approximate solution

of the minimization problem

$$\min_{\mathbf{s} \in \mathbb{R}^n} \mathcal{F}_\gamma(\mathbf{s}) \quad \text{subject to the restriction (62),} \quad (63)$$

where  $\mathcal{F}_\gamma$  is given by the expression (61) together with (58) and (59).

Starting from an initial guess  $\mathbf{s}_0 \in \mathbb{R}^n$ , which corresponds to the undistorted natural state of the body, we generate a sequence of approximate solutions  $\mathbf{s}_k \in \mathbb{R}^n$ ,  $k = 0, 1, 2, \dots$ , denoted by  $\{\mathbf{s}_k\}$ , using the recursive formula

$$\mathbf{s}_{k+1} = \mathbf{s}_k + \alpha_k \mathbf{d}_k, \quad (64)$$

where  $\alpha_k$  is a scalar minimizing  $\mathcal{F}_\gamma$  in a given direction of search  $\mathbf{d}_k$ . Procedures to obtain both  $\alpha_k$  and  $\mathbf{d}_k$  are described below.

The scalar  $\alpha_k$  is a solution of the (unidirectional) minimization problem

$$\min_{\alpha \in \mathbb{R}} \mathcal{H}(\alpha) \equiv \min_{\alpha \in \mathbb{R}} \mathcal{F}_\gamma(\mathbf{s}_k + \alpha \mathbf{d}_k),$$

which is highly nonlinear and is solved iteratively using a standard Newton–Raphson technique. The technique is based on the assumption that we can approximate  $\mathcal{H}(\alpha)$  by a quadratic function obtained from the sum of the first three terms of a Taylor series expansion of  $\mathcal{H}(\alpha)$  about the minimizer  $\alpha_k$ . We assume that  $\alpha^{(0)} = 0$  is a good initial guess for  $\alpha_k$ . By minimizing the quadratic function, we generate the estimate  $\alpha^{(1)}$ , which is taken as the next guess for  $\alpha_k$ . By repeating this process, we arrive at the recursive formula

$$\alpha^{(i+1)} = \alpha^{(i)} - \frac{\mathcal{H}'(\alpha^{(i)})}{\mathcal{H}''(\alpha^{(i)})}, \quad \alpha^{(0)} = 0, \quad i = 0, 1, \dots \quad (65)$$

We then generate the sequence  $\{\alpha^{(i+1)}\}$ ,  $i = 0, 1, \dots$ , which is expected to converge to  $\alpha_k$  as the number of elements in the sequence tends to infinity [Aguar 2006].

For each  $\alpha^{(i+1)}$  calculated from (65), we check the signs of the nodal values of the discrete injectivity constraint, given by (62), to make sure that they are all positive for  $\mathbf{s} = \mathbf{s}_k + \alpha^{(i+1)} \mathbf{d}_k$ . This is the only place in the whole numerical scheme where we check for constraint violations.

To determine a direction of search  $\mathbf{d}_k$  in (64), we consider that, in a vicinity of  $\mathbf{s}_k$ , the scalar function  $\mathcal{F}_\gamma$  can be approximated by the quadratic form

$$\mathcal{F}_\gamma(\mathbf{s}) \approx \mathcal{Q}_n(\mathbf{s}) \equiv \mathcal{F}_\gamma(\mathbf{s}_k) + \nabla_{\mathbf{s}} \mathcal{F}_\gamma(\mathbf{s}_k) \cdot (\mathbf{s} - \mathbf{s}_k) + \frac{1}{2} (\mathbf{s} - \mathbf{s}_k) \cdot \nabla_{\mathbf{s}}^2 \mathcal{F}_\gamma(\mathbf{s}_k) (\mathbf{s} - \mathbf{s}_k),$$

where  $\nabla_{\mathbf{s}} \mathcal{F}_\gamma \equiv (\partial \mathcal{F}_\gamma / \partial \eta_1, \partial \mathcal{F}_\gamma / \partial \eta_2, \dots, \partial \mathcal{F}_\gamma / \partial \eta_n)$  is the gradient of  $\mathcal{F}_\gamma$  and  $\nabla_{\mathbf{s}}^2 \mathcal{F}_\gamma$  is the Hessian of  $\mathcal{F}_\gamma$ . By solving the equation  $\nabla_{\mathbf{s}} \mathcal{Q}_n(\mathbf{s}) = 0$ , which is a necessary condition for the existence of a minimizer  $\hat{\mathbf{s}}$  of the quadratic form  $\mathcal{Q}_n$ , we obtain

$$\mathbf{d}_k \equiv \hat{\mathbf{s}} - \mathbf{s}_k = - [\nabla_{\mathbf{s}}^2 \mathcal{F}_\gamma(\mathbf{s}_k)]^{-1} \nabla_{\mathbf{s}} \mathcal{F}_\gamma(\mathbf{s}_k), \quad k = 0, 1, \dots$$

The sequence of limit points  $\{\mathbf{s}_k\}$  generated by (64) converges to the solution  $\mathbf{r}_\gamma \in \mathbb{R}^n$  of the discrete minimization problem (63).

Next, we increase the penalty parameter  $\gamma$  and repeat the whole minimization process outlined above. Now, however, we start the new minimization process taking for  $\mathbf{s}_0$  the limit point  $\mathbf{r}_\gamma$  of the previous minimization process. The initial direction of search  $\mathbf{d}_0$  is the direction of steepest descent evaluated at

the new point  $\mathbf{s}_0$ . Using this procedure for a fixed  $h$ , we generate a sequence  $\{\mathbf{r}_\gamma\}$  that converges to a limit point  $\mathbf{r}_h \in \mathbb{R}^n$  as  $\gamma \rightarrow \infty$ . We use  $\mathbf{r}_h$  together with the representation (56) to construct the function  $\mathbf{u}_h = (\mathbf{r}_h \cdot \mathbf{g})\mathbf{e}_\rho$ . This function is an approximation of the solution  $\mathbf{u}$  of the original problem (1)–(3) for a fixed  $h$ . Letting  $h \rightarrow 0$ , we generate a sequence  $\{\mathbf{u}_h\}$  that converges to  $\mathbf{u}$ .

The algorithm for the minimization problem  $\min_{\mathbf{s} \in \mathbb{R}^n} \mathcal{F}_\delta(\mathbf{s})$ , where  $\mathcal{F}_\delta$  is given by (61)b together with (58) and (60), is similar to the algorithm described above. Here, however, we let  $\delta \rightarrow 0$  in order to generate a sequence  $\{\mathbf{r}_\delta\}$  that converges to the limit point  $\mathbf{r}_h \in \mathbb{R}^n$ . Also, we do not need to check the signs of the nodal values of the discrete injectivity constraint, given by (62), since the minimization is performed over all  $\mathbf{s} \in \mathbb{R}^n$ .

### 5. Numerical results

We apply the numerical method presented in Section 4 to solve numerically the constrained pipe problem described in Section 3.2. We have normalized all lengths by setting the radius of the pipe  $\rho_e = 1$ . Furthermore, in dimensionless units, the inner radius of the pipe is  $\rho_i = 0.001$ , the elastic constants are  $c_{11} = 10^5$ ,  $c_{22} = 10^3$ , and  $c_{12} = 10^3$ , and the applied load on the boundary of the pipe is  $p = 500$ . With these geometric and material parameters, we find from (25), (34)b, (35)a, b, (38), and (39) that  $\kappa = 0.1 < 1$ ,  $\hat{p} = 0.005$ ,  $p_1 \cong 0.00132$ ,  $\mu_\theta = 0.01$ ,  $p_2 \cong 0.00359$ , and  $p_c \cong 1.76913$ , respectively. Recall from Section 3 that  $p_1$  is the value of  $\hat{p}$  below which  $1 + u'(\rho)$  is positive and no self-intersection occurs,  $p_2$  is the value of  $\hat{p}$  above which we have two roots for the algebraic equation  $1 + u(\rho)/\rho = 0$ , and  $p_c$  is an upper bound for  $\hat{p}$ . Then, the roots of the algebraic equations  $1 + u'(\rho) = 0$  and  $1 + u(\rho)/\rho = 0$ , where  $u$  is the unconstrained solution given by the expression (34) together with (35), are given by  $\rho_1 \cong 0.00381$ ,  $\rho_A \cong 0.00148$ , and  $\rho_B \cong 0.00784$ . Also, we take  $\varepsilon = 0.1$  for the lower bound of the injectivity constraint<sup>1</sup>. The radius of the core subregion  $\mathcal{B}_=$  where the constraint is active is calculated from (48) together with (49), yielding  $\rho_a \cong 0.00554$ , and the value of  $\hat{p}$  above which  $\det(\mathbf{1} + \nabla \mathbf{u}) = \varepsilon$  in  $[\rho_i, \rho_e]$  is calculated from (51), yielding  $p_0 = 0.69061$ .

In Figure 2 we show two graphs for the determinant of the deformation gradient  $J \equiv \det(\mathbf{1} + \nabla \mathbf{u})$  calculated from the exact solutions of both the constrained pipe problem, represented by the solid line, and the unconstrained pipe problem, represented by the dashed line. The graph on the left side refers to the entire interval, whereas the graph on the right side refers to a neighborhood of the inner surface of the pipe. Observe from the graph on the left that, away from the inner surface, both curves are close to each other and from the graph on the right that  $J$ , obtained from the unconstrained solution, vanishes at the radii  $\rho_A$ ,  $\rho_1$ , and  $\rho_B$ , whereas  $J$ , obtained from the constrained solution, is constant in  $[\rho_i, \rho_a]$ , increasing thereafter.

The numerical solutions were obtained with nonuniform partitions of the interval  $(0, \rho_e)$  in such a way that the coarsest partition has 300 elements in  $(0, 0.07\rho_e)$ , 100 elements in  $(0.07\rho_e, 0.46\rho_e)$ , and 80 elements in  $(0.46\rho_e, \rho_e)^2$ , totaling 480 elements. The other partitions are obtained from the coarse partition by multiplying the number of elements of this partition by integer powers of 2. Thus, the most

<sup>1</sup> These geometric and material parameters are used by Fosdick and Royer-Carfagni [2001] in their analytical study of the compressed disk problem.

<sup>2</sup> The nonuniform mesh of 480 elements is similar to the mesh used by Obeidat et al. [2001] in their computational study of the compressed disk problem.

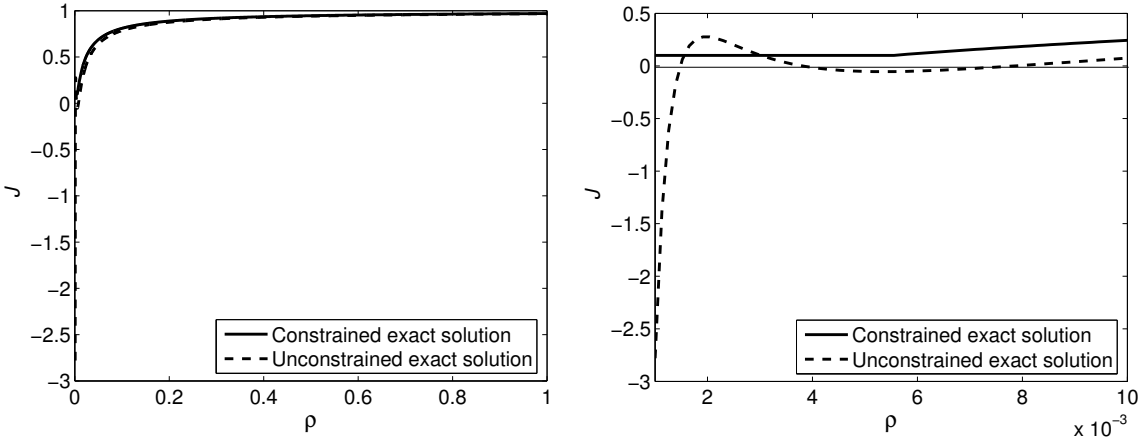


**Figure 2.** Determinant of the deformation gradient  $J \equiv \det(\mathbf{1} + \nabla \mathbf{u})$  versus radius  $\rho$  for both the constrained and unconstrained pipe problems.

refined mesh has  $2^4 \times 480$  elements, totaling 7680 elements. In what follows, the characteristic length  $h$  is the length of the largest interval and  $n$  is the total number of elements. Also, we increase the penalty parameter  $\gamma$  in (61)a by powers of 10, that is, we consider  $\gamma = 10, 10^2, \dots$ , and we decrease the penalty parameter  $\delta$  in (61)b by negative powers of 10, meaning we consider  $\delta = 10^{-1}, 10^{-2}, \dots$ .

In Figure 3 we show two graphs with both the exact analytical solution, given by (46) and (47) and represented by the solid line, and the numerical solutions, obtained with the nonuniform mesh of 7680 elements and represented by the dash-dotted lines. The graph on the left side was obtained with the interior penalty formulation using increasing values of  $\gamma$  and the graph on the right side was obtained with the exterior penalty formulation using decreasing values of  $\delta$ . We see from both graphs that the sequences of numerical solutions converge to limit functions that cannot be distinguished from the analytical solution.

In Figure 4 we show curves for the base 10 logarithm of the Euclidean norm of the error  $e$  between the exact solution  $\mathbf{u} = u\mathbf{e}_\rho$ , given by (46) together with (47), and the numerical solution  $\mathbf{u}_h = (\mathbf{r}_h \cdot \mathbf{g})\mathbf{e}_\rho$ ,

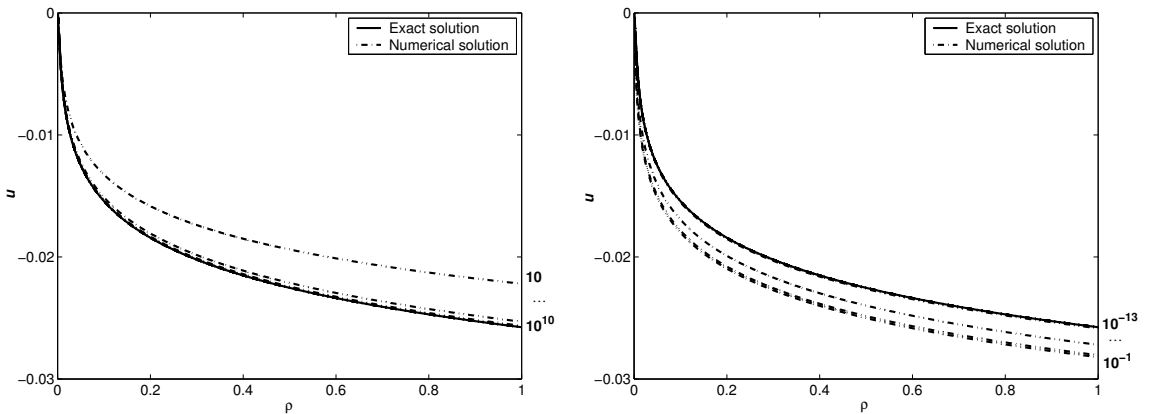


**Figure 3.** Radial displacement  $u$  versus radius  $\rho$  for the constrained pipe problem with  $n = 7680$ . Left:  $\gamma = 10, \dots, 10^{10}$ . Right:  $\delta = 10^{-1}, \dots, 10^{-13}$ .

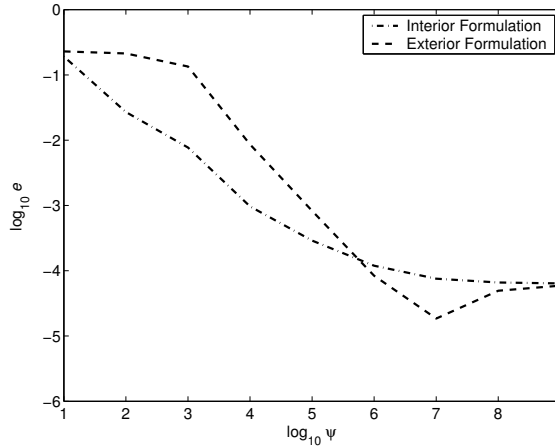


**Figure 4.** Base 10 logarithm of the error  $e \equiv \|\mathbf{r} - \mathbf{r}_h\|_2$  versus base 10 logarithm of the penalty parameter  $\psi$ , where  $\psi$  is either  $\gamma$  or  $1/\delta$ .

obtained from the most refined mesh of 7680 elements. This error is plotted against the base 10 logarithm of the penalty parameter  $\psi$ , which is equal to  $\gamma$  for the interior penalty formulation (dash-dotted line) and is equal to  $1/\delta$  for the exterior penalty formulation (dashed line). Observe from the dash-dotted line that  $\log_{10} e$  decreases monotonically with increasing values of  $\gamma$  and tends to an asymptotic value as  $\gamma$  becomes large. A different behavior is observed for the dashed line. Here,  $\log_{10} e$  is almost constant for small and large values of  $1/\delta$  and decreases rapidly in an interval of intermediate values of  $1/\delta$ . For small  $1/\delta$ , the penalty part in (61) is not enforced and the numerical solution is a good approximation of the solution for the unconstrained pipe problem of Section 3.1. Thus, for small  $1/\delta$ ,  $e$  is the approximate error between the unconstrained and constrained solutions.

In both curves shown in Figure 4 we see that the errors tend to asymptotic values as both  $\gamma$  and  $1/\delta$  tend to infinity. In Figure 5 we consider different discretizations and show curves for the base 10 logarithm of the Euclidean error  $\|\mathbf{r}_b - \mathbf{r}_h\|_2$  between the best numerical solution  $u_b \equiv \mathbf{r}_b \cdot \mathbf{g}$ , obtained with large values of either  $\gamma$  or  $1/\delta$  for each discretization, and the numerical solution  $u_h = \mathbf{r}_h \cdot \mathbf{g}$ . This error is plotted against both the base 10 logarithm of the parameter  $\gamma$  in the graph on the left side and the base 10 logarithm of the parameter  $1/\delta$  in the graph on the right side.

Observing the graph on the left side of Figure 5, we see that  $\|\mathbf{r}_b - \mathbf{r}_h\|_2$  decreases monotonically with increasing values of  $\gamma$  and that all the curves are similar to each other. In particular, notice that all these curves are almost straight lines for large values of  $\gamma$ . Performing a linear regression on the curve corresponding to 7680 elements, represented by the dash-dotted line, we find that the angular coefficient is approximately equal to  $-0.73717$ , which corresponds to a convergence ratio<sup>3</sup> of  $10^{-0.73717} \cong 0.18$ . Similar analysis can be performed on the curves shown in the graph on the right side of Figure 5. Observe from this graph that all the curves are almost straight lines for  $1/\delta \geq 10^6$ . For these values of  $\delta$ , the angular coefficient obtained from a linear regression analysis of the curve corresponding to 7680 elements is approximately equal to  $-0.52206$ , which corresponds to a convergence ratio of  $10^{-0.52206} \cong 0.30$ .

<sup>3</sup>Consider the ratio between two consecutive values of a sequence of real numbers. If this ratio tends to a constant value as the number of terms in the sequence tends to infinity, then the ratio is called the convergence ratio of the sequence.

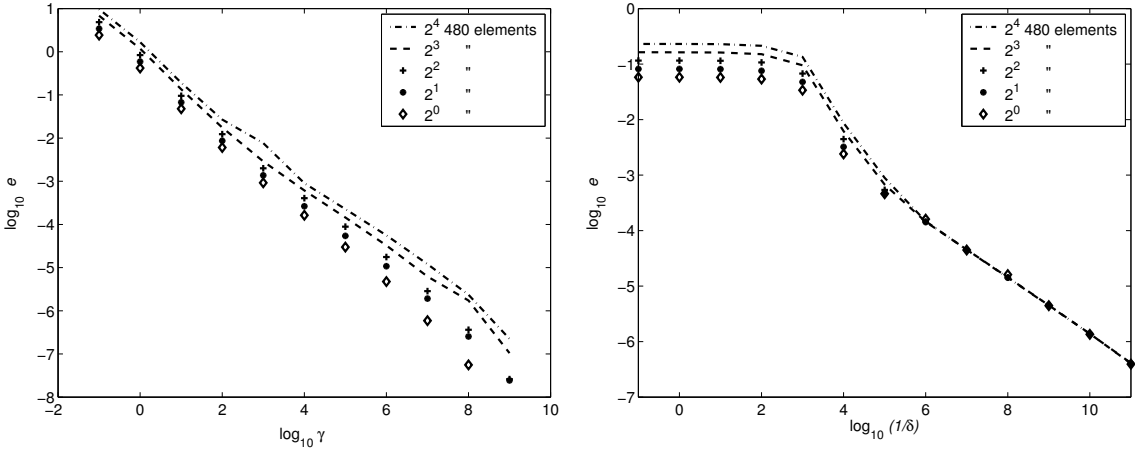


**Figure 5.** Base 10 logarithm of the Euclidean error  $e = \|\mathbf{r}_b - \mathbf{r}_h\|_2$  versus base 10 logarithm of the parameter a)  $\gamma$  (left), b)  $1/\delta$  (right).

We see from the this that, for sufficiently large  $n$ , the sequence of numerical solutions parameterized by  $\gamma$  converges faster to a limit function than the sequence of numerical solutions parameterized by  $\delta$ . Also, this convergence is more uniform for the sequence of solutions parameterized by  $\gamma$  than it is for the sequence of solutions parameterized by  $\delta$ . In particular, notice that this last sequence yields a convergence ratio close to one for small values of  $1/\delta$ . To quantify this, we performed a linear regression analysis on the curve corresponding to 7680 elements for  $1/\delta < 10$  and found that the angular coefficient is approximately equal to  $-0.01045$ , which corresponds to a convergence ratio of  $10^{-0.01045} \cong 0.98$ .

Next, we chose the largest value of  $\gamma$  in the interior penalty formulation for each discretization and obtained the numerical solutions represented by the dash-dotted lines in Figure 6. Observe from the graph

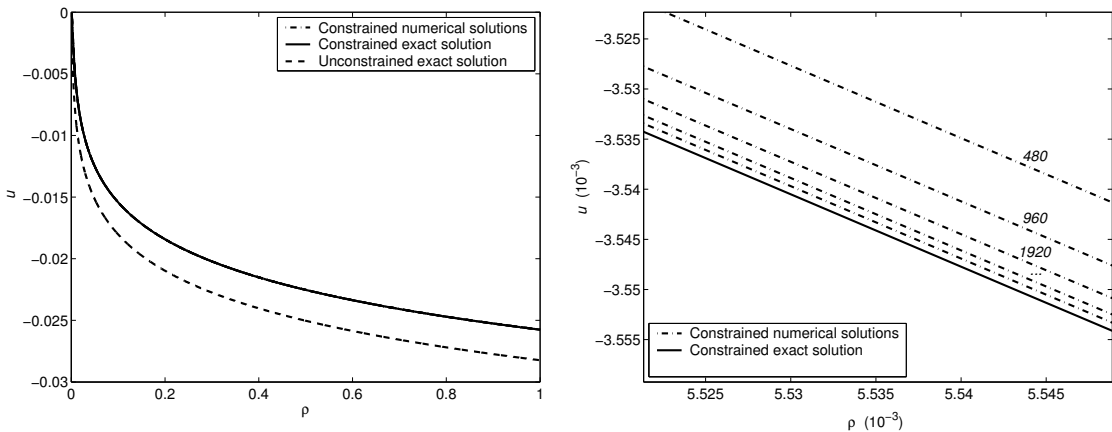


**Figure 6.** Radial displacement  $u$  versus radius  $\rho$  for the constrained pipe problem for either large  $\gamma$  or small  $\delta$  and for an increasing number of elements. Left: Interval  $(\rho_i, \rho_e)$ . Right: Magnified view showing the distinction between the numerical solutions and the exact solution.

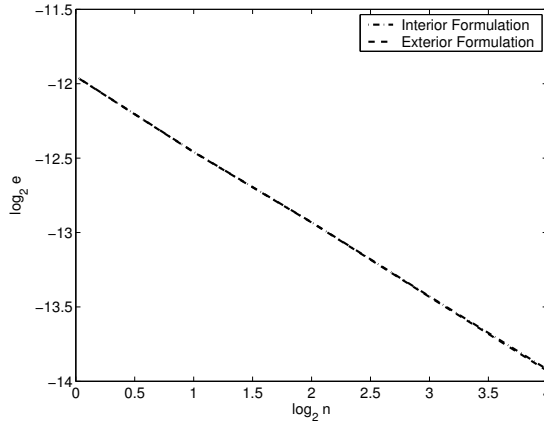


**Figure 7.** Base 2 logarithm of the Euclidean error  $e$  versus base 2 logarithm of the number of elements  $n$  for either large  $\gamma$  or small  $\delta$ . Both curves are indistinguishable at this scale.

on the left side of this figure that the numerical solutions are not distinguishable from the constrained exact solution, given by (46) together with (47) and represented by the solid line. We also show in this graph the unconstrained exact solution, which is given by (34) and (35) and is represented by the dashed line. By comparing this line with the solid line, we conclude that the imposition of the injective constraint has the effect of stiffening the material. Similar conclusions are reached by Aguiar [2006] and Fosdick and Royer-Carfagni [2001] in their treatment of radially symmetric constrained problems.

The graph in Figure 6, right, corresponds to a zoom in a neighborhood of  $\rho = \rho_a$ . Here, we can see that the sequence of numerical solutions obtained with increasing  $n$  converges to the constrained exact solution. At this scale, it is not possible to see the dashed line corresponding to the unconstrained exact solution. Identical curves were obtained using the exterior penalty formulation with a fixed small  $\delta$ .

In Figure 7 we show curves for the base 2 logarithm of Euclidean norm of the error between the exact solution  $\mathbf{u} = u\mathbf{e}_\rho$ , given by (46) and (47), and the numerical solution  $\mathbf{u}_h = (\mathbf{r}_h \cdot \mathbf{g})\mathbf{e}_\rho$  versus the base 2 logarithm of the number of elements  $n$ . The dash-dotted line corresponds to the numerical solution obtained with the interior formulation and the dashed line corresponds to the numerical solution obtained with the exterior formulation. Observe from the figure that both curves are on the top of each other and are almost straight lines. Observe also that the error decreases with the increasing number of elements. Performing a linear regression on these curves, we found that the angular coefficients are approximately equal to  $-0.49316$ , which corresponds to a convergence ratio of  $2^{-0.49316} \cong 0.7105$ .

In Figure 8 we show the determinant of the deformation gradient  $J \equiv \det(\mathbf{1} + \nabla \mathbf{u})$  calculated from both the exact solution of the constrained pipe problem, represented by the solid line, and the corresponding numerical approximations. These approximations, which are represented in the figure by different line styles, were obtained using both the interior penalty formulation with large  $\gamma$  and the nonuniform meshes. The graph on the left in Figure 8 refers to the entire interval, whereas the graph on the right refers to a neighborhood of the inner surface of the pipe which contains the active region, that is, for  $\rho \in (\rho_i, \rho_a)$ . Observe from the graph on the left the very good agreement between the analytical and the numerical results and from the graph on the right that the numerical approximations of  $J$  converge to the analytical

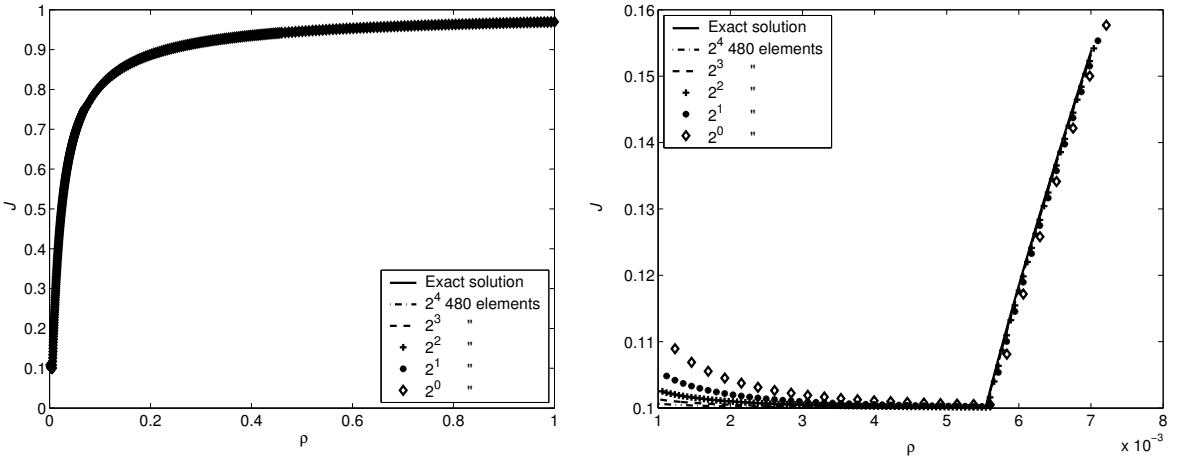


**Figure 8.** Determinant of the deformation gradient  $J \equiv \det(\mathbf{1} + \nabla \mathbf{u})$  versus radius  $\rho$  for the constrained pipe problem using large  $\gamma$ .

solution as the mesh is refined. In particular, observe from this last graph that the numerical scheme captures well the sharp change in  $J$  at  $\rho = \rho_a$ . Identical curves were obtained using the exterior penalty formulation.

In Figure 9 we show the determinant of the deformation gradient  $J \equiv \det(\mathbf{1} + \nabla \mathbf{u})$  calculated from both the exact solution of the constrained pipe problem, represented by the solid line, and its numerical approximations, represented by the dash-dotted line, for the most refined mesh of 7680 elements. The graphs on the left and the right sides of Figure 9 refer to the approximations obtained with, respectively, the interior and the exterior penalty formulations. Observe from both graphs that  $J_h$  converges to a limit function as the penalty parameter is enforced in each case, that is, as  $\gamma \rightarrow \infty$  on the left graph and as  $\delta \rightarrow 0$  on the right graph. Recall from the analysis of Figure 8 that both limit functions are identical, are represented by the dash-dotted line in the graph on the right of that figure, and approximate the analytical solution  $J = \varepsilon$  (recall,  $\varepsilon = 0.1$ ) in the interval  $(\rho_i, \rho_a)$ .

Observe from the graph on the right side of Figure 9 that, in the interval  $(\rho_i, \rho_a)$ , the approximations  $u_h$  of the minimizer  $u$  lie in the exterior of the set  $\mathcal{A}_\varepsilon$  for large  $\delta$  since, in this case,  $J_h < \varepsilon$ . Nevertheless, contrary to what one might expect, as  $\delta \rightarrow 0$ , the sequence of approximations  $\{u_h\}$  converges to a limit function that belongs to the constrained set  $\mathcal{A}_\varepsilon$ .

### 6. Conclusion

In this work we investigate the problem of equilibrium of a circular homogeneous and cylindrically orthotropic pipe that is fixed at its inner surface, is radially compressed along its outer surface, and is subjected to an axial force on its flat ends. In the classical linear theory, the solution to this problem is smooth everywhere, including the boundary of the pipe, and predicts self-intersection in a neighborhood of the inner surface for a sufficiently large, but reasonable, compressive radial pressure. Of course, this behavior has no physical meaning. By using a minimization theory that enforces the injectivity condition  $J \geq \varepsilon > 0$ , where  $J$  is defined in the expression (31) and  $\varepsilon$  is small, we obtain a radially symmetric solution

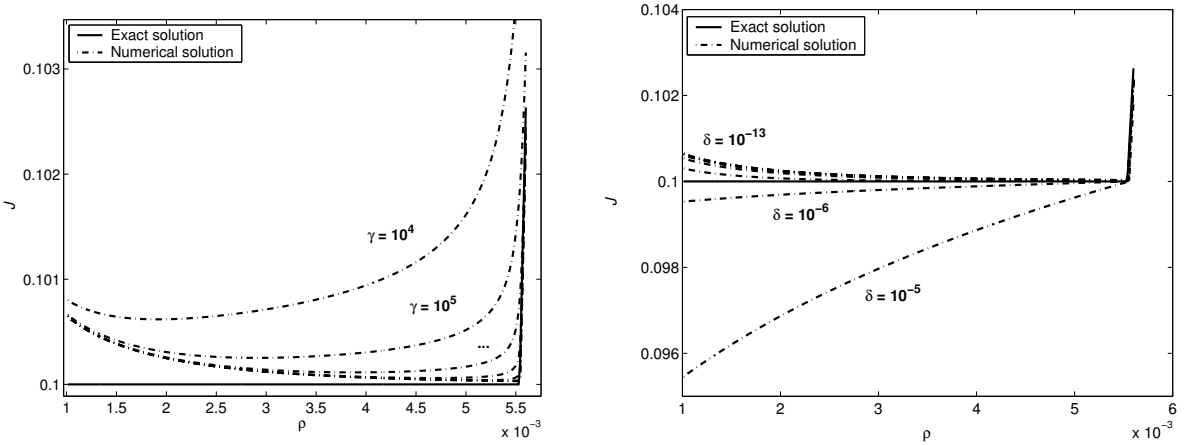


**Figure 9.** Determinant of the deformation gradient  $J \equiv \det(\mathbf{1} + \nabla \mathbf{u})$  versus radius  $\rho$  for the constrained pipe problem using  $n = 7680$ . Interior (left) and exterior (right) penalty formulations.

to the corresponding constrained minimization problem that satisfies this injectivity condition, as shown in Figure 2, that does not predict the anomalous self-intersecting behavior anywhere in the pipe, and that yields a stiffer material response.

The advantage of investigating radially symmetric one-dimensional problems is that, in general, their solutions are known in the context of both unconstrained and constrained minimization theories of quadratic functionals [Fosdick and Royer-Carfagni 2001; Aguiar 2006]. A disadvantage of this investigative approach is that not all possible solutions of the corresponding full two-dimensional problems can be obtained in the context of the constrained theory (see, for instance, the numerical treatment of a full two-dimensional problem by Fosdick et al. [2008]).

We then use both an interior and an exterior penalty formulation of the constrained minimization problem together with a standard finite element method and classical nonlinear programming techniques to find approximate solutions to this constrained problem. We show numerical results obtained from discrete versions of both formulations that are in very good agreement with analytical results presented in Section 3.2. We highlight below the main findings from the analysis of these results.

- (1) For a given finite element mesh, the sequences of numerical results obtained with both penalty formulations converge to the same limit function as the penalization is enforced (see Figures 6 and 7). These sequences are, however, very different from each other (see Figure 3) and converge at different rates (see Figures 4 and 5).
- (2) For a given finite element mesh, the results shown in Figure 5 indicate that the interior penalty formulation yields a sequence of numerical solutions that converges faster and more uniformly to a limit function than the sequence obtained from the exterior penalty formulation.
- (3) For a given finite element mesh, a sequence of numerical solutions  $u_\psi$ , where either  $\psi = \gamma$  for the interior penalty formulation or  $\psi = 1/\delta$  for the exterior penalty formulation, yields a convergent sequence of  $J_\psi = \det(\mathbf{1} + \nabla \mathbf{u}_\psi)$  that satisfies  $J_\psi \geq \varepsilon$  everywhere in the pipe as  $\psi \rightarrow \infty$  (see Figure 8).

(4) The interior formulation yields, expectedly,  $J_\gamma \geq \varepsilon$  for every  $\gamma > 0$  (see Figure 9 on the left) and the exterior formulation yields  $J_{1/\delta} < \varepsilon$  in  $(0, \rho_a)$  for large  $\delta$  and  $J_{1/\delta} \geq \varepsilon$  in  $(0, \rho_a)$  for small  $\delta$  (see Figure 9 on the right). This last result was not expected, because, in general, the exterior formulation yields a sequence of penalized solutions that converges to the solution of the problem from the exterior of the constrained set. Here, however, the sequence is converging from the interior of the set as  $1/\delta \rightarrow \infty$ .

In summary, both penalty methods are viable methods of analysis for the class of constrained minimization problems considered in Section 2, lead to simple numerical schemes that yield very accurate approximate solutions to the corresponding constrained problems, and can be used to solve more complex problems. The main advantage of the exterior penalty method is that the corresponding minimization problem is unconstrained. Also, the exterior penalty functional chosen in this work, given by the expression (13), leads to a penalty function  $\mathcal{F}_\delta$ , given by (61)b together with (58) and (60), that is differentiable everywhere. On the other hand, the main findings highlighted above suggest that, given a finite element mesh, the interior penalty method yields a sequence of numerical solutions that converges faster and more uniformly to a limit function than the sequence obtained from the exterior penalty method. In addition, the numerical solutions obtained with the interior penalty method are kinematically admissible for any penalty parameter.

This work is part of an ongoing research effort to determine the best strategy to tackle general higher dimensional singular problems in elasticity for which the corresponding solution may exhibit self-intersection in the vicinity of corners and crack tips. The results obtained in this work suggest that the best strategy might be a combination of both penalty formulations. One might use the interior penalty formulation to generate a numerical solution that is a good approximation to the solution of the constrained problem and then use this numerical solution as the initial guess in the search of the constrained solution with the exterior penalty formulation.

### Appendix

Here, we resolve the technical issue that arose in the solution (45) for the Lagrange multiplier function  $\hat{\lambda}(\rho)$ .

**Proposition.** To be consistent with  $\hat{\lambda}(\rho) \geq 0$  in  $(\rho_i, \rho_a)$ , the jump of  $u'$  across  $\rho = \rho_a$  must be zero and  $\tilde{\rho} = \rho_a$ .

*Proof.* We consider a procedure that is analogous to the procedure used by [Fosdick and Royer-Carfagni 2001] in the analysis of a model problem that is a particular case of our problem when  $\rho_i = 0$ .

First, we rewrite the expression (45) as

$$\hat{\lambda}(\rho) = -\frac{\rho_i^2(\tilde{\rho}^2 - \rho^2)(1 - \varepsilon)\varepsilon}{2[g(\rho)g(\tilde{\rho})]^2} + \log\left(\frac{h(\rho)}{h(\tilde{\rho})}\right), \quad \rho \in (\rho_i, \rho_a), \tag{A.1}$$

where

$$h(\rho) = \frac{g(\rho)}{\rho^{\kappa^2}[\sqrt{\varepsilon}\rho + g(\rho)]^\alpha}, \quad \alpha \equiv \frac{(1 - \kappa^2)}{\sqrt{\varepsilon}}. \tag{A.2}$$

Next, we substitute the expressions (44), (A.1), and (A.2) in the jump condition (43)b to obtain

$$\log\left(\frac{h(\rho_a)}{h(\tilde{\rho})}\right) = -\frac{\rho_a}{g(\rho_a)} \left| [u'(\rho_a)] \right| + \frac{\rho_i^2(\tilde{\rho}^2 - \rho_a^2)(1 - \varepsilon)\varepsilon}{2[g(\rho_a)g(\tilde{\rho})]^2}, \quad (\text{A.3})$$

where  $|[u'(\rho_a)]| \equiv u'(\rho_a^+) - u'(\rho_a^-)$  is the jump of  $u'$  across  $\rho = \rho_a$ .

Noting that  $\log(h(\rho)/h(\tilde{\rho})) = \log(h(\rho)/h(\rho_a)) + \log(h(\rho_a)/h(\tilde{\rho}))$  and using (A.3) in (A.1), we can rewrite  $\hat{\lambda}$  as

$$\hat{\lambda}(\rho) = -\frac{\rho_i^2(\rho_a^2 - \rho^2)(1 - \varepsilon)\varepsilon}{2[g(\rho)g(\rho_a)]^2} + \log\left(\frac{h(\rho)}{h(\rho_a)}\right) - \frac{\rho_a}{g(\rho_a^-)} \left| [u'(\rho_a)] \right|. \quad (\text{A.4})$$

Since  $\hat{\lambda}(\rho_a) \geq 0$ , we see from (A.4) that  $|[u'(\rho_a)]| \leq 0$ , which implies that

$$u'(\rho_a^+) \leq u'(\rho_a^-). \quad (\text{A.5})$$

On the other hand, the condition  $\det \nabla \mathbf{f} \geq \varepsilon$  in  $(\rho_a, \rho_e)$  together with the expressions (31), (28), and  $\varepsilon_3 = 0$ , yields  $(1 + u'(\rho_a^+))(1 + u(\rho_a^+)/\rho_a) \geq \varepsilon$ . Also,  $(1 + u'(\rho))(1 + u(\rho)/\rho) = \varepsilon$  for  $\rho \in (\rho_i, \rho_a)$ . Since  $u(\rho_a^+) = u(\rho_a^-)$  from the jump condition (43)a, we then find that

$$u'(\rho_a^+) \geq u'(\rho_a^-). \quad (\text{A.6})$$

Thus, it follows from both (A.5) and (A.6) that  $|[u'(\rho_a)]| = 0$ .  $\square$

**Acknowledgements.** The author wishes to acknowledge Fundação de Amparo à Pesquisa do Estado de São Paulo (FAPESP), proc. # 2007/03753-9, and the University of Minnesota Supercomputing Institute (UMSI) for their support of this research.

## References

- [Aguiar 2006] A. R. Aguiar, “Local and global injective solution of the rotationally symmetric sphere problem”, *J. Elasticity* **84**:2 (2006), 99–129.
- [Aguiar and Fosdick 2001] A. R. Aguiar and R. L. Fosdick, “Self-intersection in elasticity”, *Int. J. Solids Struct.* **38**:28–29 (2001), 4797–4823.
- [Christensen 1994] R. M. Christensen, “Properties of carbon fibers”, *J. Mech. Phys. Solids* **42**:4 (1994), 681–695.
- [Fosdick and Royer-Carfagni 2001] R. L. Fosdick and G. Royer-Carfagni, “The constraint of local injectivity in linear elasticity theory”, *Proc. R. Soc. Lond. A* **457**:2013 (2001), 2167–2187.
- [Fosdick et al. 2008] R. L. Fosdick, F. Freddi, and G. Royer-Carfagni, “Bifurcation instability in linear elasticity with the constraint of local injectivity”, *J. Elasticity* **90**:1 (2008), 99–126.
- [Lekhnitskii 1968] S. G. Lekhnitskii, *Anisotropic plates*, Gordon and Breach, New York, 1968.
- [Obeidat et al. 2001] K. Obeidat, H. Stolarski, R. Fosdick, and G. Royer-Carfagni, “Numerical analysis of elastic problems with injectivity constraints”, in *Solids, structures and coupled problems in engineering: 2nd European Conference on Computational Mechanics (ECCM-2001); proceedings* (Cracow, 2001), Politechnika Krakowska, Cracow, 2001. On CD.
- [Tarn 2002] J.-Q. Tarn, “Stress singularity in an elastic cylinder of cylindrically anisotropic materials”, *J. Elasticity* **69**:1–3 (2002), 1–13.
- [Tings 1999] T. C. T. Tings, “New solutions to pressuring, shearing, torsion, and extension of a cylindrically anisotropic elastic circular tube or bar”, *Proc. R. Soc. Lond. A* **455**:1989 (1999), 3527–3542.

Received 21 Jan 2008. Revised 15 May 2008. Accepted 6 Aug 2008.

ADAIR R. AGUIAR: [aguiarar@sc.usp.br](mailto:aguiarar@sc.usp.br)

*Department of Structural Engineering, São Carlos School of Engineering, University of São Paulo, Av. Trabalhador  
São-carlense, 400, 13566-590 São Carlos, SP, Brazil*

<http://www.set.eesc.usp.br/public/pessoas/professor.php?id=2>

ROGER L. FOSDICK: [fosdick@aem.umn.edu](mailto:fosdick@aem.umn.edu)

*Aerospace Engineering and Mechanics, University of Minnesota, 107 Akerman Hall, 110 Union St. SE, Minneapolis, MN  
55455-0153, United States*

<http://www.aem.umn.edu/people/faculty/bio/fosdick.shtml>

JESÚS A. G. SÁNCHEZ: [jesusg@sc.usp.br](mailto:jesusg@sc.usp.br)

*Department of Structural Engineering, São Carlos School of Engineering, University of São Paulo, Av. Trabalhador  
São-carlense, 400, 13566-590 São Carlos, SP, Brazil*

